2,4,6-Trinitro-*N*-(*m*-tolyl)aniline: A New Polymorphic Material Exhibiting Different Colors

Bernardo A. Nogueira,[1,2,*] Susana M. M. Lopes,[1] Susy Lopes,[1] Timur Nikitin,[1]
Ana Clara B. Rodrigues,[1] Maria Ermelinda S. Eusébio,[1] José A. Paixão,[3]
Teresa M. V. D. Pinho e Melo,[1] Alberto Milani,[2] Chiara Castiglioni[2] and Rui Fausto[1]

[1] *University of Coimbra, CQC-IMS, Department of Chemistry, P-3004-535 Coimbra, Portugal.*
[2] *CMIC, Dipartimento di Chimica, Materiali e Ingegneria Chimica "G. Natta", Politecnico di Milano, Italy.*
[3] *University of Coimbra, CFisUC, Department of Physics, P-3004-516 Coimbra, Portugal*

Abstract

2,4,6-Trinitro-*N*-(*m*-tolyl)aniline or *N*-picryl-*m*-toluidine (abbreviated as TMA), exhibiting color polymorphism, was synthesized and characterized structurally, spectroscopically and thermodynamically. The studies consider both the isolated molecule of the compound (studied theoretically at the DFT(B3LYP)/6-311++G(d,p) level, and experimentally by matrix isolation infrared spectroscopy) and its polymorphic crystalline phases. The investigations on the isolated molecule allowed to evaluate the major intramolecular interactions determining the conformational preferences of the compound, and characterize it in detail from the vibrational point of view. Two conformers were found (A and B), which differ in the relative orientation of the ring moieties of the molecule. Polymorph screening, by recrystallization of the compound using different solvents, allowed to identify three different polymorphs, exhibiting red, orange and yellow colors, which were subsequently characterized structurally by single crystal X-ray diffraction, vibrationally, by infrared and Raman spectroscopies (complemented by fully-periodic DFT calculations on the crystals), electronically, using solid state ultraviolet-visible absorption spectroscopy, and thermodynamically, by differential scanning calorimetry and polarized light thermomicroscopy. The yellow polymorph was found to be a conformational polymorph of the orange and red ones, while the last two are packing polymorphs. Mechanistic insights on the causes of the different colors of the polymorphs are presented. On the whole, the reported investigation constitutes a comprehensive structural (for both the isolated molecule and crystalline phases), spectroscopic and thermal analysis of the newly prepared compound, with particular emphasis on the rare color polymorphism it exhibits.

Keywords: 2,4,6-trinitro-*N*-(*m*-tolyl)aniline, color polymorphism, molecular structure, crystal structure, thermal analysis, infrared, Raman and UV-Vis spectroscopies

* Corresponding author e-mail: ban@qui.uc.pt

1. Introduction

From the Greek *poly* (many) and *morph* (form), polymorphism refers, in the crystallographic context, to the ability of a compound to exist in more than one crystalline structure.[1,2] Polymorphs, despite being composed by the same compound, present different physical, chemical and mechanical properties. This fact makes polymorphic materials interesting (and challenging) chemical systems from a fundamental perspective (*e.g.*, as ideal objects to investigate crystallization and the factors affecting crystallization), while it is also on the basis of their attractiveness for application in various fields, in particular in dyes, agrochemicals, pigment and pharmaceutical industries.[1–3]

There are two main types of polymorphism, the conformational polymorphism and the packing polymorphism. The first implies the existence of different conformers of the same compound in the different polymorphs (a new conformer is obtained every time the variation of torsion angles in a molecule leads to a region of the molecule's potential energy surface that is associated with a new minimum that is structurally not equivalent to the original one).[1,4] On the other hand, packing polymorphism relates to polymorphs that are constituted by the same conformer.[1,4] In the case of conformational polymorphism, the intermolecular forces are strong enough to supersede the intramolecular forces and stabilize, in the crystalline state, conformers that are not the conformational ground state for the isolated molecule. In contrast, in the case of the packing polymorphism, most frequently intramolecular forces determine the conformer which is present in the different polymorphs. This is in general the most stable conformer found for the isolated molecule, but the selection of a higher-energy form upon crystallization is not a rare phenomenon. In both types of polymorphism (conformational and packing), intermolecular interactions are distinct in the different polymorphs; in the case of conformational polymorphism, both inter- and intramolecular interactions are essentially different from polymorph to polymorph and, together, determine the dissimilar properties of the polymorphs.[1,2,5–7]

Color polymorphism is the term used to define a compound presenting either conformational or packing polymorphs that display different color.[1] It is a rather uncommon property of polymorphic systems, and that is why, in spite of their relevant potential applications in several areas, like in pigments and sensors industries, for example,[8–11] the number of known compounds exhibiting color polymorphism is still very limited.[12–21]

In this work, we describe a compound that presents color polymorphism. The compound, 2,4,6-trinitro-*N*-(*m*-tolyl)aniline ($C_{13}H_{10}N_4O_6$, or *N*-picryl-*m*-toluidine; Scheme 1, abbreviated TMA) is made by the combination of a picryl moiety with a *meta*-toluidine ring, and it is a close parent of the previously investigated *para*-toluidine analogue, 2,4,6-trinitro-*N*-(*p*-tolyl)aniline (or *N*-picryl-*p*-toluidine; Scheme 1). *N*-picryl-*p*-toluidine was reported for the first time in 1909, by Busch and Pungs, and its color polymorphism is known since then.[18] Subsequent studies on this compound allowed for the determination of the crystal structures of its orange-yellow and dark-red polymorphs, and the investigation of their interconversion.[22–26] The color polymorphism in *N*-picryl-*p*-toluidine is a typical

case of packing polymorphism, where the same conformer is present in the different polymorphs.[1] Very interestingly, as it is shown in the present article, the synthesized *N*-picryl-*m*-toluidine analogue gives rise to 3 different polymorphs, which show both packing and conformational types of color polymorphism. The different position of the methyl group in the toluidine ring, which favors a larger number of conformers resulting from the rotation about the $N–C_{(tolyl)}$ bond in the case of the presently studied *m*-substituted molecule, compared to the *p*-substituted compound previously investigated, is the main structural reason justifying the different behavior of the two compounds regarding the number of polymorphs and type of structural relation between them.

TMA

Scheme 1 – 2,4,6-Trinitro-*N*-(*m*-tolyl)aniline (TMA; left), and 2,4,6-trinitro-*N*-(*p*-tolyl)aniline (right).

In the next sections of this article, we will present the details of the synthesis of TMA, followed by the theoretical characterization of its conformational space using the DFT method, and the subsequent investigation of the isolated molecules of the compound trapped into a cryogenic inert matrix, by infrared spectroscopy. The interpretation of the spectroscopic results is supported by the comparison of the experimentally obtained spectra with those predicted theoretically for the experimentally relevant conformers. These investigations on the isolated molecule shed light on the major intramolecular interactions determining the conformational preferences of the compound. Then, the results of the performed polymorph screening, by recrystallization of the compound using different solvents, are presented. Three different polymorphs, exhibiting red, orange and yellow colors, were obtained, which were afterward characterized structurally by single crystal X-ray diffraction, vibrationally, by infrared and Raman spectroscopies (complemented by fully-periodic DFT calculations on the crystals), electronically, using solid state ultraviolet-visible (UV-visible) absorption spectroscopy, and thermodynamically, by differential scanning calorimetry (DSC) and polarized light thermomicroscopy (PLTM). On the whole, the reported investigation constitutes a comprehensive structural (for both the isolated molecule and crystalline phases), spectroscopic and thermal analysis of the studied compound, with particular emphasis on the rare color polymorphism it exhibits.

2. Experimental and Computational Methods and Instrumentation

2.1. Experimental methods and instrumentation

The reagents and solvents were obtained commercially with analytical grade. For the initial characterization of the synthesized compound, the ^{1}H and ^{13}C NMR spectra (Figure S1, in

the Supporting Information) were recorded on a Bruker Avance III instrument, operating at 400 MHz and at 100 MHz, respectively. The solvent used was deuterochloroform. The infrared (IR) spectrum (Figure S2) was recorded on an Agilent Cary 630 FTIR Fourier transform spectrometer, with a diamond-based attenuated total reflection (ATR) cell (Smart Orbit). Melting point (uncorrected) was determined in an open glass capillary. Elemental analysis was carried out with an Elemental Vario MicroCube analyzer. Thin-layer chromatography (TLC) analyses were performed using precoated silica gel plates.

The cryogenic matrices were prepared by co-deposition of vapors of the studied compound together with a large excess of the matrix host-gas [Ar (N60) obtained from Air Liquide] onto a CsI substrate placed at the cold (15 K) tip of the cryostat (ARS Cryogenics closed-cycle helium refrigeration system, with a DE-202SI expander). The solid compound was sublimated from a homemade Knudsen cell, the calve nozzle being kept at room temperature. The temperature of the CsI window was measured directly at the sample holder by a silicon diode sensor, connected to a digital temperature controller (LakeShore 335 Temperature Controller), which provides an accuracy of 0.1 K. The IR spectrum of the matrix-isolated compound, in the 4000−400 cm^{-1} range, was obtained using a Thermo Nicolet iS50 Fourier transform infrared spectrometer equipped with an MCT/A detector and a KBr beam splitter, with 0.5 cm^{-1} spectral resolution and 256 scans. To avoid interference from atmospheric H_2O and CO_2, a stream of dry CO_2-filtered air was continuously purging the optical path of the spectrometer.

The different polymorphs of TMA were obtained by recrystallization with the slow evaporation of different solvents at room temperature. 30 mg of the compound were dissolved in 5–10 mL of the solvent, depending on the solubility, the solutions were filtered to prevent any crystal seed and the solvent left to evaporate at room temperature. The solvents used were toluene, 1,4-dioxane, tetrahydrofuran (THF), dichloromethane, chloroform, carbon tetrachloride, acetone, butanone, dimethyl sulfoxide (DMSO), ethyl acetate, formic acid, acetic acid, methanol, ethanol, 1-propanol, dimethylformamide (DMF) and acetonitrile.

The infrared spectra of the polymorphs were collected in the attenuated total reflectance (ATR) mode, using a Thermo Scientific FT-IR Nicolet iS5 system, with an iD7 ATR accessory (angle of incidence: 45; crystal: diamond). The spectra were recorded in the wavenumber range of 400–4000 cm^{-1}, with spectral resolution of 1 cm^{-1}, being the average of 512 scans. The Raman spectra were obtained with 4 cm^{-1} resolution, in the 50–3350 cm^{-1} wavenumber range, with 785 nm excitation provided by a solid-state laser, using a BWTEK i-Raman Pro instrument, equipped with a CCD detector. The spectra were collected using a 20× magnification objective, the exposure time of 10 seconds, with 10 accumulations, and a laser power at the sample of ~4 mW, to prevent thermal degradation of the sample.

The single crystal X-ray diffraction experiments were performed at room temperature using graphite monochromated MoKα (λ = 0.71073 Å) radiation in a Bruker APEX II diffractometer. The structure was solved by the dual-space algorithm implemented in SHELXT-2018/2, and full-matrix

least-squares refinement of the structural model was performed using SHELXL-2018/3. All non-hydrogen atoms were refined anisotropically. Hydrogen atoms were placed at calculated idealized positions and refined as riding using SHELXL-2018/3 default values,[27] except for those of the N−H group that were refined isotropically with a displacement parameter constrained to 1.2x their parent atoms.

Full details on data collection and structure refinement are provided in the Supporting Information (Crystallographic Data). A summary of the data collection and refinement details is given in Table 1. CIF files containing the supplementary crystallographic data were deposited at the Cambridge Crystallographic Data Centre, with reference CCDC 2100574 (yellow polymorph), 2100587 (red polymorph) and 2100671 (orange polymorph).

Table 1 – Summary of the single-crystal X-ray data collection and crystal structure refinement.

Chemical formula	$C_{13}H_{10}N_4O_6$		
Formula weight	318.25		
Color, shape	yellow/plate	orange/plate	red/block
Space group	$P2_1/c$	$Pna2_1$	P-1
Temperature(K)	292(2)	294(2)	292(2)
Cell volume (Å^3)	681.42(4)	1388.0(3)	681.42(4)
Crystal system	monoclinic	orthorhombic	triclinic
a (Å)	12.5800(7)	29.971(3)	7.5195(2)
b (Å)	8.0014(4)	9.0537(10)	8.3723(3)
c (Å)	15.0156(8)	5.1150(6)	12.2263(4)
α (deg)	90	90	81.0389(19)
β (deg)	110.794(2)	90	81.9157(18)
ɣ (deg)	90	90	64.0565(17)
$Z/Z´$	4/1	4/1	2/1
D_c (Mg m^{-3})	1.496	1.523	1.551
Radiation (Å) (graphite, monochromated)	0.71073	0.71073	0.71073
Max. crystal dimensions (mm)	0.53×0..45×0.18	0.43×0.35×0.19	0.25×0.19×0.17
Θ range (deg)	1.732-27.496	2.350-27.497	3.257-27.482
Range of h, k, l	–16,16;–10,10;–19,19	–38,38;–11,11;–6,6	–9,9;–10,10;–15;15
Reflections measured/independent	26093/3250	39121/3190	53896/3125
Reflections observed ($I > 2\ \sigma$)	1931	2141	2031
Data/restraints/parameters	3250/0/212	3190/1/212/	3125/0/212
GOF	1.029	1.046	1.035
R_1 ($I > 2\ \sigma$)	0.0532	0.0448	0.0556
wR_2	0.1613	0.1054	0.1714
Function minimized	$\Sigma\ w\ (\|F_o\|^2 - S\|F_c\|^2)$	$\Sigma\ w\ (\|F_o\|^2 - S\|F_c\|^2)$	$\Sigma\ w\ (\|F_o\|^2 - S\|F_c\|^2)$
Diff. density final max/min (e Å^{-3})	0.255, –0.253	0.202, –0.176	0.426, –0.269

DSC experiments were performed using a PerkinElmer Pyris-1 power compensation calorimeter, with a 1:1 v/v ethylene glycol-water cooler at −25 °C and a 20 mL min^{-1} nitrogen purge flow. Hermetically sealed aluminium pans were used (samples weighting between 1 and 2 mg), with an empty pan used as reference. Indium (PerkinElmer, 99.99%, T_{fus} = 156.60 °C) and biphenyl (CRM LGC, T_{fus} = 68.93 °C ± 0.03 °C) were used for temperature and enthalpy calibrations. In the experiments, the samples were scanned from 25 to 140 °C at a scan rate of 10 °C min^{-1}. Polarized light thermal microscopy (PLTM) images (200×) were obtained within the range of temperature of the DSC experiments on a system that includes a DSC600 Linkam hot stage attached to a Leica DMRB microscope.

The absorption spectra of the crystalline samples were recorded by collecting diffuse reflectance using an Agilent Cary 5000 DRA UV-vis-NIR spectrometer, with an integrating sphere accessory with detection in the 200–2500 nm range. The background correction was performed by collecting the baseline with 0% and 100% reflectance (using a blocked beam and a polytetrafluoroethylene reference sample, respectively) before the collection of the spectra of the investigated samples. The conversion to absorption was performed assuming the Kubelka-Munk function.[28] The color parameters were determined according to the CIE (Commission Internationale de l'Eclairage proceedings) 1931 scale diagram.[29] The *x* and *y* color parameters were determined from the transmittance spectra acquired on the Agilent Cary 5000 DRA UV-Vis-NIR spectrometer.

2.2. Computational details

The density functional theory (DFT) calculations performed on the isolated molecule of the compound, including the geometry optimization, the dihedral coordinate scan, and the vibrational spectra of the different conformers of the studied molecule were carried out using the Gaussian 09 program.[30] Specifically, the three-parameter B3LYP density functional, with the Becke's gradient exchange correction[31] and the Lee, Yang and Parr correlation functional,[32] was used together with the 6-311++G(d,p) basis set.[33] Calculated frequencies for the monomeric species were scaled by 0.982.

The full geometry optimization of the crystal structures and prediction of IR and Raman spectra of the three polymorphs of the studied compound were carried out using the CRYSTAL17[34,35] code, within the DFT framework. To test the accuracy of different functionals and basis sets, the B3LYP[31,32] and PBE0[36] hybrid exchange–correlation functionals were used, together with the 6-31G(d,p) basis set. The empirical correction for dispersion interaction (DFT-D) developed by Grimme[37–39] was also employed to consider van der Waals and other dispersion attractive interaction forces. In all calculations, the atomic positions and the lattice parameters were fully optimized. The input structures for the calculations were those experimentally determined and presented in this work. The vibrational frequencies calculations at the Γ point have been performed on the optimized geometries, as achieved by the diagonalization of the numerically calculated Hessian matrices. All predicted frequencies were scaled by a single empirical factor (0.9512)[40] to allow a better comparison with the experimental data.

3. Results and Discussion

3.1. Synthesis of the compound and characterization of the obtained material

2,4,6-Trinitro-*N*-(*m*-tolyl)aniline (TMA) was prepared by the condensation of *m*-toluidine with 1-chloro-2,4,6-trinitrobenzene (Scheme 2), under conditions adapted from literature.[41] Sodium acetate anhydrous (0.170 g, 2.07 mmol) and *m*-toluidine (0.222 mL, 2.07 mmol) were added to a stirred solution of 1-chloro-2,4,6-trinitrobenzene (0.512 g, 2.07 mmol) in ethanol (15 mL). The reaction mixture was stirred at room temperature for 2 h (monitored by TLC). The precipitated product was filtered, washed with 30% aqueous solution of ethanol and dried under vacuum to give an orange solid (0.490 g, 75%). mp 120.0–121.8 ºC (from ethanol). IR (ATR) ν 735, 1090, 1173, 1293, 1336, 1507, 1530, 1591, 1602, 1620 and 3293 cm^{-1}. ^1H NMR δ ($CDCl_3$): 2.34 (s, 3H), 6.87-6.88 (m, 2H), 7.10 (d, J =7.6 Hz, 1H), 7.25-7.29 (m, 1H), 9.09 (s, 2H), 10.28 (br s, 1H). ^{13}C NMR δ ($CDCl_3$): 21.4, 118.0, 121.5, 127.2, 128.6, 129.8, 137.2, 137.9, 139.0, 140.3. Anal. Calc. for $C_{13}H_{10}N_4O_6$: C 49.06, H 3.17, N 17.61. Found: C 49.07, H 3.03, N 17.59. Only one polymorph, of orange color, was obtained directly from the synthetic procedure.

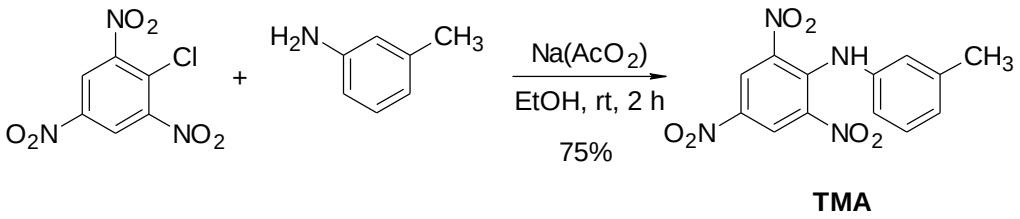

Scheme 2 – Synthesis of 2,4,6-trinitro-*N*-(*m*-tolyl)aniline (TMA).

3.2. DFT calculations and matrix-isolation IR investigation of the TMA isolated molecule

The molecule of the studied compound has three *a priori* conformationally relevant coordinates, which are associated with the internal rotations about the $C_{(picryl)}$–N and N–$C_{(tolyl)}$ bonds of the bridge, and the rotation of the methyl group. However, the presence of the two nitro groups in the picryl moiety *ortho* to the $C_{(picryl)}$–N bond leads to a strong conformational preference for structures where the picryl–NH fragment is nearly planar, due to the establishment of an intramolecular hydrogen bond of N–H···O type, forming a *pseudo*-6-membered ring. Since the conformation of the picryl–NH moiety is determined by this reason, the internal rotation around the N–$C_{(tolyl)}$ bond becomes the single conformationally relevant coordinate associated with the bridging group.

A series of relaxed scan calculations was then performed, where the 4C–1N–7C–12C dihedral angle was chosen as driving coordinate, varying by increments of ±10º, while all other internal coordinates were optimized. Potential energy profiles corresponding to rotations in the two directions (clockwise and anti-clockwise) were computed, and are depicted in Figure 1. The starting geometry and the direction of the rotation influence the obtained energy profiles by the reasons explained below.

Altogether, the obtained energy profiles allowed for identification of two pairs of equivalent-by-symmetry conformers (herein-after referred to as conformers A/A' and B/B', or just A and B when there are no doubts of the meaning of the abbreviated version; see Figure 2). Figure 3 shows the potential energy profiles for methyl group rotation in each one of the conformers.

The potential energy plots shown in Figure 1 are very interesting. Along the rotation of the tolyl moiety around the 1N–7C bond, the orientation of the non-hydrogen-bonded *ortho*-nitro group has to change, in order to avoid steric hindrance when the tolyl group tries to approach co-planarity with the picryl moiety. Inversion at the amino bridge nitrogen atom also occurs during the scans. Hence, when the scan starts at the geometry of the minimum B, corresponding to a 4C–1N–7C–12C dihedral angle of 144.0º, using steps of –10º, the molecule first crosses the B→A isomerization barrier (which amounts to 13.0 kJ mol^{-1}), and reaches the global minimum (conformer A; 4C–1N–7C–12C of 40.4º), which stays 0.5 kJ mol^{-1} below the energy conformer B. Then, the energy progressively raises to a value of 37.5 kJ mol^{-1}, which occurs for a dihedral angle of ca. –56.0º, where the change of orientation of the non-hydrogen-bonded *ortho*-nitro group takes place together with the inversion at the nitrogen of the amine bridge, so that energy reduces abruptly. Continuation of the scan after this point, leads to the B' minimum by overcoming the A'→B' conformational transition. The subsequent scan from B' in the direction of B follows a similar pattern, with the energy growing progressively till reaching the position at which an abrupt energy decrease takes place due to the change of the conformation of the non-hydrogen-bonded *ortho*-nitro group and inversion at the nitrogen of the amine bridge, at a position corresponding to a 4C–1N–7C–12C dihedral angle of ca. 124.0º, which is already smaller than that of B. Hence, the scan starting from B for decreasing values of the 4C–1N–7C–12C dihedral angle does not allow to reach the minimum A', but only A and B', and it does not return to the initial minimum B when moving from B'. However, it shall be noticed that these findings do not mean that the different minima do not interconvert. Indeed, for example, after the abrupt change in the geometry taking place at ca. –56.0º, the molecule still reaches the potential energy well of A', so that the conversion between A and A' can effectively occur in practice (the same can be stated for the conversion between B' and B). If the scan is performed in the opposite direction, identical conclusions can be drawn, both regarding the format of the potential energy profile along the scan, and about the real possibility of conversion between A' and A, on one side, and B and B' on the other. The scans starting at the position of the global minimum A yield identical results.

Taking into account the results discussed above, the barrier for interconversion between conformer A and B (and their equivalent forms, A' and B') is of 13.5 kJ mol^{-1} (13.0 kJ mol^{-1} in the reverse direction) and those between the symmetry-related forms of both conformers, A and A', and B and B', are 37.5 and 30 kJ mol^{-1}, respectively. Conformer A is predicted to be only 0.5 kJ mol^{-1} more stable than conformer B, which in practical terms means that they are nearly iso-energetic. In both conformers, the *para* and the *ortho*-hydrogen bonded nitro groups are nearly coplanar with the aromatic ring to which they are bound (these two groups are tilted out of the plane of the ring by 0.1 and 11.0º

respectively, in both conformers), while the second *ortho* nitro group is tilted by –40.2 and –41.2º from the ring in conformers A and B, respectively, leading to a geometry where this group is nearly parallel to the tolyl moiety. The geometry around the intramolecular hydrogen bond is identical in both conformers, with the 5C–4C–1N–7C and 5C–4C–1N–1H dihedral angles being 154.4º and –13.4º, respectively, and the 1N–1H bond length being 1.017 Å in both conformers, and the 1H···5O distance being 1.813 and 1.811 Å in conformers A and B, respectively. The 4C–1N and 1N–7C bond lengths are also equal in the two conformers, the first being considerably shorter (1.348 Å) than the latter (1.425 Å) due to the π-electron delocalization from 1N to the picryl ring, which awards the 4C–1N a substantial double bond character.

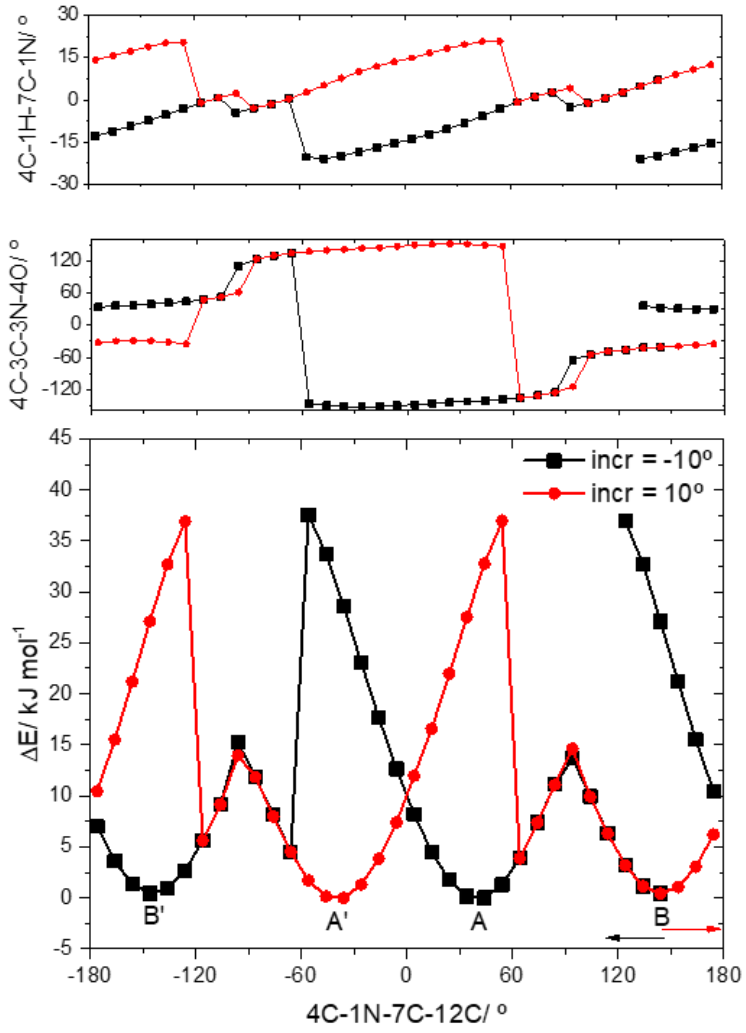

Figure 1 – Computed B3LYP/6-311++G(d,p) relaxed potential energy scans corresponding to the internal rotation around the 1N–7C bond, as defined by the 4C–1N–7C–12C torsion angle. The minima A/A' and B/B' correspond to the two pairs of symmetry-equivalent minima. The increment (incr) in the driving coordinate is equal to ±10º. The arrows indicate the direction of the scans. The top and middle panels show the variation of the pyramidalization degree at the bridging nitrogen atom (as expressed by the dihedral 4C–1H–7C–1N) and of the orientation of the non-hydrogen-bonded *ortho* nitro group along the scans.

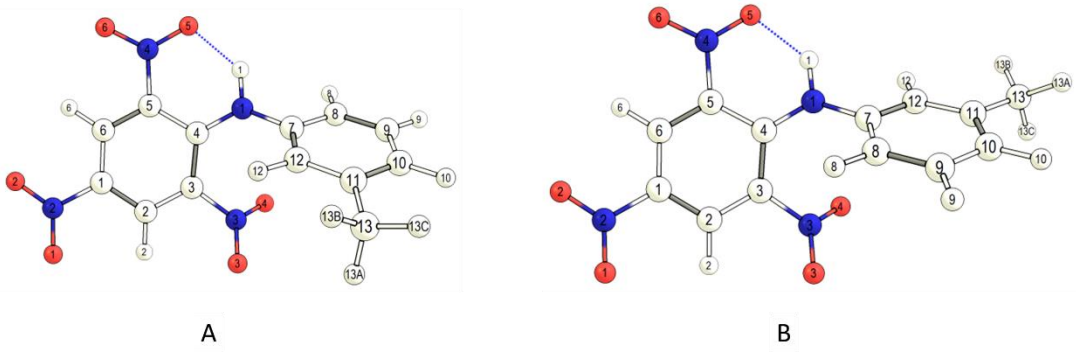

Figure 2 – Geometries of the two conformers of TMA, with atom numbering. Each of the represented structures have a symmetry-equivalent form (see Figure 1).

The orientation of the methyl group in the two conformers is slightly different (see Figure 3), though in both cases one of the hydrogen atoms stays nearly perpendicular to the ring and points roughly to the non-hydrogen-bonded *ortho* nitro group. However, in conformer A the 10C–11C–13C–H angle (97.3º) is larger than the 12C–11C–13C–H angle (i.e., the nearly perpendicular methyl hydrogen atom is turned to inside the molecule), while in conformer B the opposite trend is observed (the 10C–11C–13C–H angle is, in this case 80.6º). This structural feature is most probably due to the different importance in the two conformers of the long-range attractive interactions between the methyl group and the closest located nitro group, motivated by the rather distinct H…O(NO) distances in the two conformers (3.87 Å in conformer A vs. 5.01 Å in conformer B). It is also worth noticing that the barrier for the methyl internal rotation, though being very low in both conformers, is predicted to be nearly two-fold higher in conformer A than in conformer B (0.39 vs. 0.18 kJ mol^{-1}). This result is in consonance with the explanation given above for the different orientations of the methyl group in the two conformers, in particular the attractive nature of the long range H…O(NO) interaction, which is stronger in conformer A, thus reducing in some extent the mobility of the methyl group.

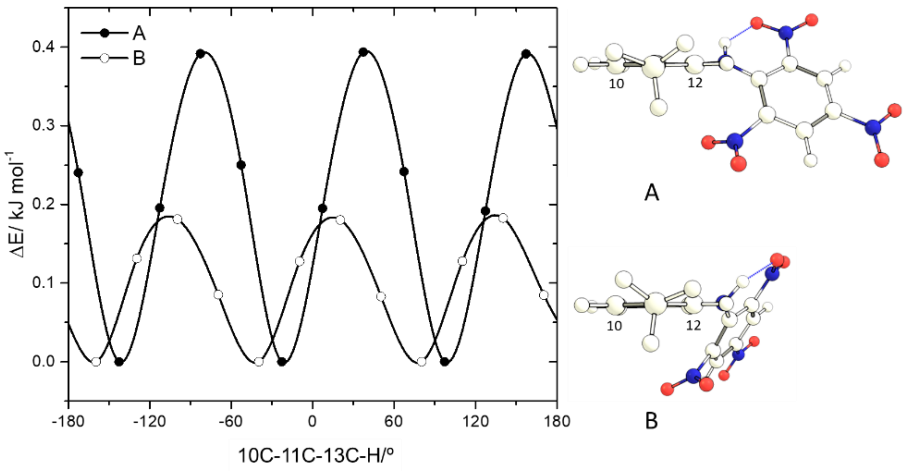

Figure 3 – Computed B3LYP/6-311++G(d,p) relaxed potential energy profile for internal rotation of the methyl group in conformers A and B.

Taking into account the results of the calculations, the populations of the two conformers in the room temperature (RT, 298.15 K) gas phase equilibrium are estimated as 54% (A) and 46% (B). The infrared spectrum of the TMA molecules trapped from the RT vapor of the compound into an argon matrix at 15 K was obtained. The registered data in the full 3600–600 cm^{-1} spectral range is provided in the Supporting Information Figure S3, while Figure 4 shows the 1700–1400 cm^{-1} region, whose analysis allows to conclude on the presence of the two conformers in the matrix in populations that match well the predicted ones.

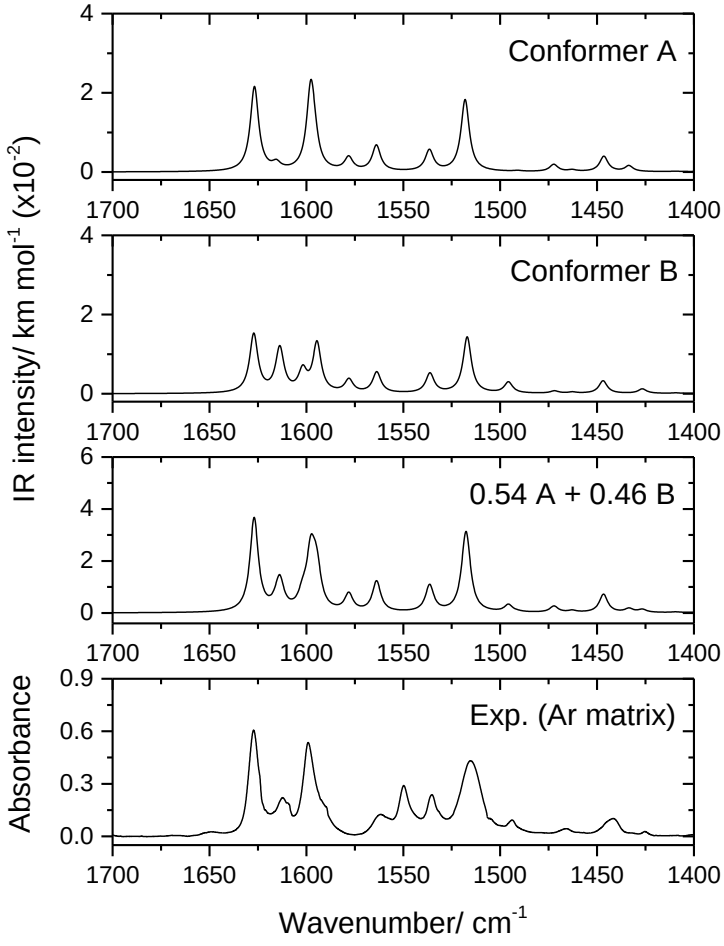

Figure 4 – Experimental infrared spectrum of monomeric TMA isolated in an argon matrix at 15 K (*bottom*), calculated spectra of conformers A and B (*top spectra*) and the simulated sum-spectrum of the conformational mixture according to the predicted room temperature Boltzmann populations. In the calculated spectra bands are represented by Lorenztian functions centered at the scaled B3LYP/6-311++G(d,p) calculated wavenumbers.

In Figure 4, the experimental spectrum can be compared with the calculated spectra of the two conformers and a spectrum built by adding these spectra with intensity scaled proportionally to the predicted relative populations of the conformers in the deposited RT equilibrium gaseous beam. It is considered here that this equilibrium is retained upon deposition, since the energy barriers separating the conformers are all large enough to prevent their interconversion during deposition.[42] Though the spectra of the two conformers are very similar, in the spectral region depicted in Figure 4 it is clear that

the population weighted spectrum fits much better the experimental spectrum than the individual spectra of each conformer. The relative intensity of the feature appearing at ca. 1611 cm^{-1} (comparing it with the neighbor bands at 1627 and 1599 cm^{-1}) is predicted for conformer A to be much less intense than that observed experimentally, while for conformer B it is too intense. On the other hand, the population weighted spectrum fits nicely to the relative intensities of these bands in the experimental spectrum. Indeed, the reproduction of the experimental data by the sum spectrum is remarkable regarding both frequencies and relative intensities (see Figure 4), even for the low intensity bands, which does not happen for the spectra of the individual conformers. For example, the band at 1494 cm^{-1}, is absent from the spectrum of conformer A, and it is then a mark-band for the less stable conformer B. Below 1400 cm^{-1}, the reproduction of the experimental spectrum by the calculated sum-spectrum is also very good, though some bands ascribable mostly to vibrations of the nitro groups have been comparatively less well predicted by the calculations (the comparatively less good prediction of the frequencies associated with the vibrations of the nitro groups can also be noticed in the spectral region depicted in Figure 4, where the experimental bands at 1562 and 1550 cm^{-1}, which have significant contributions from the NO_2 anti-symmetric stretching modes, appear slightly overestimated by the calculations.)

The good overall agreement between the experimental and calculated spectra allowed a reliable assignment of the experimental bands, which is given in Table 2 (the full calculated vibrational data for the conformers are given in the Supporting Information Tables S1 and S2). In Table 2, the bands that are ascribable to the individual conformers are highlighted.

Table 2 – Assignment of the infrared spectrum of matrix isolated (Ar, 15 K) TMA.[a]

Experimental[c]	Calculated[b]				
Ar matrix	Conformer A		Conformer B		
ν	ν	*I*	ν	*I*	Approximate description[d]
3316 A/ 3308 B	3405.4	184.2	3402.0	178.2	νNH
3107	3178.0	30.7	3179.0	30.8	νC6H
3096	3170.0	20.0	3170.2	20.7	νC2H
3056	3137.8	7.4	3136.2	4.7	νC8/9/10H s
3048	3124.9	11.3	3122.7	11.0	νC8/9/10H as
3034	3112.2	3.2	3110.3	4.4	νC8/9/10H as’
3034	3111.7	5.1	3116.1	3.3	νC12H
2989	3052.6	14.7	3052.5	12.6	νCH_3 as
2967	3027.1	13.7	3027.6	14.6	νCH_3 as’
2934[e]	2973.0	17.0	2973.5	23.5	νCH_3 s
1627	1626.8	397.2	1627.2	319.5	νCC ring1
1612 A/ 1610 B	1615.5	30.5	1613.7	241.6	νCC ring2, δNH
1599	1597.8	376.3	1601.9	113.2	$\nu2NO_2$ as, νCC ring1, δNH
1592 (sh)	1595.8	82.9	1594.5	268.0	νCC ring2, $\nu2NO_2$ as
1562	1578.2	62.6	1578.1	70.8	δNH, $\nu1/2/3NO_2$ as
1550	1563.9	120.8	1563.7	113.1	$\nu3NO_2$ as, δNH
1535	1536.5	98.5	1536.2	106.8	νCC ring1, $\nu1NO_2$ as, $\nu2NO_2$ as
1515, 1505 (sh)	1518.1	337.6	1517.0	306.5	νCC ring1, ν1N4C, δC2H
1490 (sh) A/ 1494 B	1490.9	3.3	1495.7	59.5	δCH ring2
1466	1472.3	33.5	1472.0	12.7	δCH_3 as
1457	1462.9	7.1	1462.7	6.4	δCH_3 as’
1445 (sh), 1442	1446.5	71.9	1446.9	69.0	νCC ring1, δNH
1432 A/ 1425 B	1433.5	26.7	1426.6	24.2	νCC ring2
1400	1409.6	1.8	1409.3	2.5	δC6H, νCC ring1
1382	1391.1	3.6	1391.0	1.7	δCH_3 s

1356	1349.6	38.7	1349.7	50.2	ν3NO_2 s, δC2H, νC3N
	1346.6	102.3	1344.8	96.7	δC6H, ν3NO_2 s, νC3N
1341	1329.9	732.1	1330.0	747.6	ν2NO_2 s, νC2N
n .obs.	1322.0	1.2	1322.9	1.2	δCH ring2
1317	1307.1	99.1	1309.6	72.6	δCH ring2
1300, 1290	1287.3	263.8	1287.7	288.7	ν4NO_2 s, δCH ring2
1280	1269.3	127.1	1269.1	124.2	ν4NO_2 s, δC2/6H, δNH
1255	1246.4	5.1	1248.9	2.4	δCC ring2, ν1N7C, ν11C13C
1188	1172.8	4.9	1174.4	3.9	δCH ring2
1188	1170.7	13.4	1171.2	14.9	δCH ring2
1172 A/ 1176 (sh) B	1156.5	119.8	1157.3	97.9	δCC ring1, νC2/3/4N s
1167 A/ 1160 B	1154.6	25.1	1152.7	48.9	δC2/6H, δC12H
1094	1096.6	16.6	1099.1	3.4	δC8/10H
1082	1077.1	84.2	1077.6	94.2	δC2/6H
1040	1043.3	5.0	1042.5	6.9	γCH_3
n. obs.	1012.0	0.5	1006.5	3.4	γCH_3’
1002	997.7	3.4	996.6	6.3	δCC ring2
982 (?)	976.1	0.0	976.5	1.0	γC8/9/10H as
956	955.2	2.5	955.4	4.1	γC2/6H as
949	951.6	13.1	947.7	19.5	δring2, γCH_3’, ν1N7C
943	939.6	18.2	939.3	14.6	γC3/6H s
940	933.2	27.2	931.8	26.6	νC2N, νC3N, δC2H
924 A/ 931 B	917.3	46.8	921.2	46.6	νC4N, δ4NO_2
897	901.4	9.7	902.6	9.5	γC8/10H as
868	871.4	8.0	871.4	8.2	γC12H
842 A/ n. obs. B	839.5	5.7	830.9	3.8	δCC ring1
826	827.8	6.5	827.5	10.4	δ2/3/4NO_2 s
793	791.5	22.8	791.7	18.2	γC8/9/10H s
774	769.5	21.6	773.6	30.7	γ3NO_2, γC8/9/10H s
751 A/ 756(?) B	748.8	13.0	753.7	7.8	γ3NO, τring1, δCC ring1
747	742.5	9.3	741.7	6.0	γ4NO, γ3NO, τring1
739	730.4	17.2	728.8	15.6	γNH, δCC ring1, δ4NO_2
722[f]	717.1	19.2	717.7	19.1	γ4NO_2, τring1
727[f]	709.6	39.8	708.9	35.8	γ2NO_2, γNH
694	696.6	20.8	695.8	20.2	γNH, τring2
680	683.6	16.3	681.7	12.1	γNH
680 A/ 670 B	680.1	17.6	674.8	25.9	τring2, γ3NO_2, δCC ring1, γNH

[a] Frequencies (ν) in cm^{-1}; calculated IR intensities (*I*) in km mol^{-1}. [b] A scaling factor of 0.982 was used for calculated frequencies. [c] sh, shoulder; n. obs, not observed; ?, uncertain. [d] ν, stretching; δ, bending, τ, torsion, γ, rocking; s, symmetric, as, anti-symmetric, ring1 and ring2 refer to the picryl and tolyl rings, respectively. [e] This is the main band ascribable to the νCH_3 s mode, while the weak bands between 2908–2947 cm^{-1} are overtones and combinations of the methyl bending vibrations in Fermi resonance with the νCH_3 s mode. [f] The proposed assignment is based on relative intensities; frequencies would lead to the opposite assignment.

3.3. Polymorphs screening, IR/Raman fingerprints of the polymorphs and X-ray structures

For polymorph screening, TMA was dissolved in different solvents, as described in Section 2.1, and the different solutions were left to slow solvent evaporation at room temperature. The crystals that were obtained in the different patches were first observed at the microscope and then analyzed by Raman and IR-ATR spectroscopies.

Crystals of different colors were obtained from the recrystallizations. Yellow crystals were obtained in the recrystallizations using carbon tetrachloride, toluene, butanone, 1-propanol and ethanol, orange crystals from dimethyl formamide (DMF), acetonitrile, acetic acid, 1,4-dioxane, ethyl acetate, chloroform and tetrahydrofuran (THF), and red crystals from dimethyl sulfoxide (DMSO). Recrystallization from acetone yielded both yellow and red crystals, while recrystallization from methanol produced red and orange crystals, and a mixture of yellow and orange crystals was obtained in the recrystallization using formic acid. The attempt to produce crystals upon recrystallization in

dichloromethane failed and, instead, amorphous droplets of TMA were obtained. The crystals of the different polymorphs exhibit different habits (Figure 5), the yellow (Y) and orange (O) crystals appearing as plaques (elongated in the case of the orange variety), and the red ones (R) being block shape. The Raman and IR-ATR spectra of the three polymorphs were obtained, and are provided Figures S4 and S5 (Supporting Information). Selected regions where the spectra of the polymorphs differ more are presented in Figures 6 and 7.

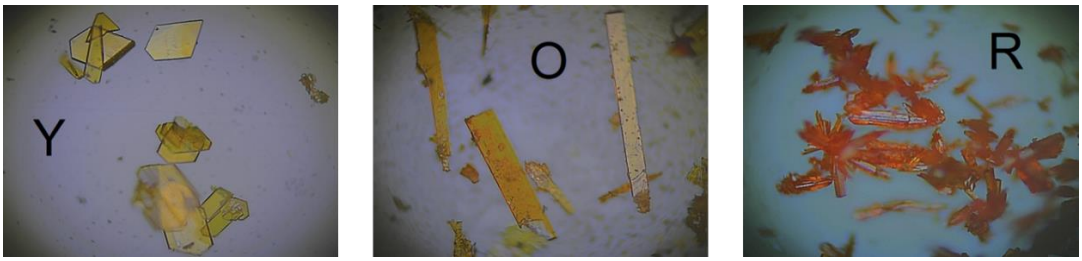

Figure 5 – Photographs of yellow (recrystallized in carbon tetrachloride), orange (recrystallized in DMF) and red (recrystallized in DMSO) crystals of TMA, with 20× magnification.

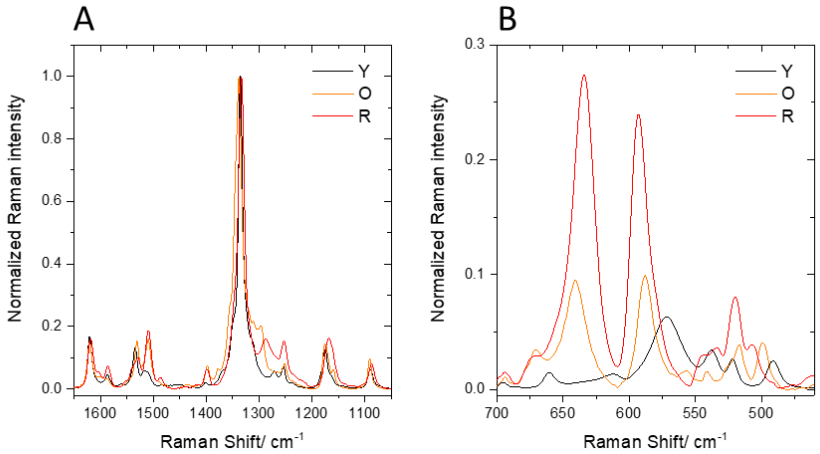

Figure 6 – Benchmark regions of the Raman spectra of the yellow (Y), orange (O) and red (R) crystals of TMA. Spectra were normalized to the peak intensity of the most intense band near 1335 cm^{-1}.

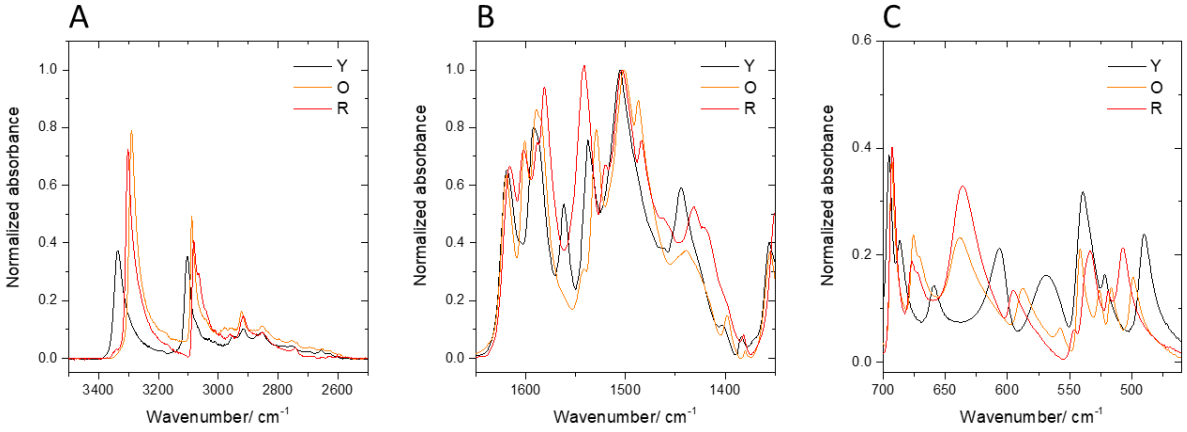

Figure 7 – Benchmark regions of the IR-ATR spectra of the yellow (Y), orange (O) and red (R) polymorphs of TMA. Spectra were normalized to the peak intensity of the band near 1505 cm^{-1}.

Both the Raman and IR-ATR spectra of the different polymorphs are significantly distinct, allowing for their simple discrimination, with the spectra of the yellow polymorph differing more from those of the orange and red polymorphs than the spectra of these latter from each other. This later result can be taken as an indication of the greater structural similarity of the orange and red polymorphs, compared to the yellow form.

The most intense band observed in the Raman spectra of the three polymorphs is due to the NO_2 symmetric stretching mode of the nitro group in *para* position to the picryl moiety. The band is observed at clearly distinguishable frequencies in the three polymorphs: 1335 (Y), 1338 (O) and 1333 (R) cm^{-1}. Considering its much higher intensity compared to all the other bands in the Raman spectra of the polymorphs (see Figure 6 A), this band is the best possible marker for polymorph fast identification, even in experimental conditions that might not allow spectra of good quality to be obtained. The bands appearing as low-frequency satellites of this band are also good indicators for polymorph identification, with the yellow polymorph showing two bands in this region (at 1271 and 1254 cm^{-1}), the orange polymorph a group of three bands at 1311, 1297 and 1252 cm^{-1}, and the red polymorph a pair of bands centered at 1287 and 1253 cm^{-1}. In addition, the bands at ca. 1510 and 1400 cm^{-1} show similar profiles and intensities in the O and R polymorphs, but are very much less intense in the Y polymorph, thus allowing easy distinction of this later species from the other two polymorphs.

The most intense Raman bands appearing in the 700–450 cm^{-1} spectral range (see Figure 6 B) are also very much discriminative. The spectrum of the Y polymorph shows a single intense band at 572 cm^{-1}, while in the spectra of both the O and R forms two intense bands are observed in this region, at 641 and 589 cm^{-1} (O) and 635 and 593 cm^{-1} (R). Noteworthy, the pair of bands observed in the spectrum of R polymorph is more than twice as intense as that observed in the spectrum of the O form.

In the case of the IR-ATR spectra, the high-frequency region (see Figure 7 A), where the NH and CH stretching vibrations absorb, is very much appropriate for discrimination of the polymorphs. The NH stretching is observed at 3339, 3293 and 3304 cm^{-1}, respectively for the yellow, orange and red crystals, while the highest intensity CH stretching band (ν6CH) appears at 3105 (Y), 3090 (O) and 3083 (R) cm^{-1}. It is also interesting to note that the relative intensity of these two bands is very much different in the yellow polymorph, compared to the orange and red polymorphs. While in the former the bands are of nearly equal intensity, in the latter two polymorphs the NH stretching band is almost twice as intense as that due to the CH stretching vibration.

The 1650-1350 cm^{-1} region of the IR-ATR spectra is rather congested, but globally quite distinct in the different polymorphs (see Figure 7 B). In this spectral region the bands can be roughly grouped in 3 sets: a high frequency group, above 1570 cm^{-1}; a low frequency group, below 1520 cm^{-1}; and an intermediate set of bands, between 1570 and 1520 cm^{-1}. This grouping is very much arbitrary, but, in a certain perspective, it is a "picture" of the structure of the molecule, which has two ring-fragments linked by a small bridge that appears as the structurally most relevant element. In this analogy, the spectroscopic bridging region between 1570 and 1520 cm^{-1} is also the most relevant of the

3 sub-regions for polymorphs distinction: between 1570 and 1520 cm^{-1}, the spectrum of the yellow polymorph exhibits two intense bands at 1563 and 1538 cm^{-1}, while those of the orange and red polymorphs show only one intense band at 1531 and 1540 cm^{-1}, respectively.

In the 700–450 cm^{-1} region, the IR-ATR spectrum of the yellow polymorph is also very much different from those of the orange and red forms (see Figure 7 C). Just to mention the most evident differences: (i) around 690 cm^{-1}, the yellow polymorph gives rise to a doublet of bands (at 696 and 687 cm^{-1}), whereas the orange and red polymorphs show a single band (at 693 and 692 cm^{-1}, respectively); and (ii) the most intense bands appearing below 650 cm^{-1} are observed at 607, 579, 540 (most intense) and 490 cm^{-1} for the yellow polymorph, and at 640/636 (most intense), 588/596, 542/533 and 499/508 cm^{-1} for the orange and red crystals, respectively.

On the whole, it can be concluded that both Raman and IR-ATR spectra are good fingerprints of the polymorphs of TMA, the spectra of the orange and red polymorphs being more similar to each other than to the spectra of the yellow polymorph, which is an indication that the first two polymorphs should share more common structural features.

To perform a detailed assignment of the spectra, a computational study relying on state-of-the-art first principles fully periodic calculations was performed on all polymorphs using the X-ray determined structures discussed below. The model to be used in these calculations was first chosen by testing different combinations of functional and empirical corrections for dispersion interaction, DFT-D proposed by Grimme,[37–39] to predict the unit cell parameters. The results of this benchmarking are shown in Table S3 (Supporting Information), and led us to select the PBE0 functional with the 6-31G(d,p) basis set. The theoretically obtained spectra are shown in Figures S6-S9 and the tentative assignments are given in Tables S4 and S5, in the Supporting Information. It is worth noticing the general good description of the experimental spectra by the computations (in particular in the case of the Raman spectra). For example, the highest intensity Raman bands in the experimental spectra (Y: 1335; O: 1338; R: 1333 cm^{-1}) correspond in the calculated spectra to pairs of bands at 1380/1369 (Y), 1378/1365 (O) and 1382/1365 (R) cm^{-1}, with intensity-weighted gravity centers at 1373, 1369 and 1371 cm^{-1}, while the mark-bands observed at 572 (Y), 641 and 589 (O), and 635 and 593 (R) cm^{-1} are predicted at 579 (Y), 652 and 590 (O) and 659/640 and 584 (R) cm^{-1}, respectively.

The structures of the three polymorphs were determined by single crystal X-ray diffraction. The crystals of the yellow, orange and red polymorphs were found to belong to the monoclinic, orthorhombic and triclinic crystal systems, respectively. The monoclinic and triclinic polymorphs belong, respectively, to the centrosymmetric $P2_1/c$ and P-1 space groups, whereas the orthorhombic one crystallizes in the non-centrosymmetric $Pna2_1$ space group. The X-ray analysis confirmed that the polymorphs feature notorious differences in both molecular conformation, molecular packing and intermolecular interactions.

The molecular conformation found in the crystal structure of the yellow polymorph is close to that of conformer A described for the isolated molecule, whereas conformer B is present in both orange

and red polymorphs (Figure 8), thus confirming the indication obtained from the IR-ATR and Raman data that the yellow polymorph should have fundamental unique structural features compared to the remaining two polymorphs. As described in detail below, distinct hydrogen bonding networks are observed in the polymorphs, thus contributing to the observed preferential stabilization of a specific conformer (either A or B) in the different crystalline states.

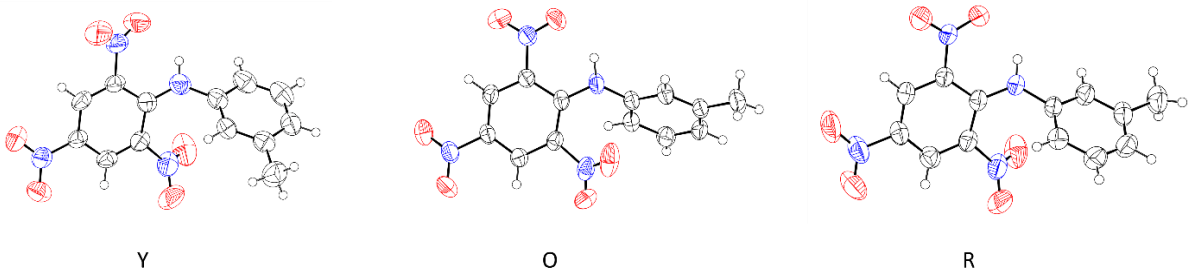

Figure 8– ORTEP plots of the monoclinic (Y, left), orthorhombic (O, centre) and triclinic (R, right) polymorphs of TMA. The anisotropic displacement ellipsoids are drawn at the 50% probability level.

Valence angles and bond distances in the molecule determined in the X-ray study are unexceptional for all polymorphs, falling within the range of expected values. The internal ring angles adjacent to the carbon atoms attached to the strong electron withdrawing NO_2 groups are significantly larger than those adjacent to unsubstituted carbon atoms (Table 3).[43] The N–O bond distances are in the range of 1.203–1.233 Å, a small lengthening being observed for the bonds involved in hydrogen-bonding, as described below.

In the three polymorphs, the angle between the least-squares planes of the two phenyl rings is similar, ranging from 53.93±0.12° (Y) up to 56.97±17° (O). The differences in molecular conformation are best put into evidence by an analysis of the torsion angles of the molecule (Table 4). Notorious differences are seen in both those angles involving rotation of the nitro groups around the $N–C_{(aryl)}$ bonds and those corresponding to the conformational flexibility of the molecule around the 1N–7C and 4C–1N bonds. As shown below, not only steric effects but also the different involvement of the NO_2 groups in the hydrogen-bonding networks of these polymorphs explain the observed differences in the torsion angles of these groups in the three polymorphs, as well as the differences to the corresponding angles calculated for the A and B conformers of the isolated molecule.

Table 3 – Valence angles in the picryl ring of the three polymorphs of TMA.

Angle/ °	Monoclinic (Y)	Orthorhombic (O)	Triclinic (R)
6C–1C–2C	120.5(2)	121.5(3)	121.5(2)
4C–5C–6C	123.8(2)	123.3(3)	123.2(2)
2C–3C–4C	123.5(2)	123.8(3)	124.1(2)
1C–2C–3C	119.8(2)	118.8(3)	118.8(6)
5C–6C–1C	119.1(2)	119.0(3)	119.2(2)
3C–4C–5C	113.2(2)	113.3(3)	113.4(2)

Table 4 – Relevant dihedral and torsion angles for the three polymorphs of TMA.

Angle/ º	Monoclinic (Y)	Orthorhombic (O)	Triclinic (R)
Torsion angle			
<(1C...6C)/(7C...12C)	53.93(12)	56.97(17)	57.85(12)
<(1C...6C)/2NO_2	–1.5(3)	17.0(4)	8.3(3)
<(1C...6C)/3NO_2	41.5(3)	40.3(5)	48.2(4)
<(1C...6C)/4NO_2	31.4(3)	18.9(4)	13.6(3)
Dihedral angle			
2C–1C–2N–1O	1.2(3)	15.6(5)	7.8(4)
4C–3C–3N–4O	–38.9(4)	38.6(5)	–44.8(4)
6C–5C–4N–6O	30.3(5)	–16.6(5)	12.8(3)
5C–4C–1N–7C	147.8(3)	–150.7(4)	153.0(2)
4C–1N–7C–12C	152.8(3)	–142.4(4)	143.5(3)

The three polymorphs show quite distinct hydrogen-bonding patterns, depicted in Figure 9, with details given in Table 5. Like for the isolated molecule of the compound, in the three polymorphs a strong intramolecular hydrogen bond is established between the amine 1N–1H group of the bridge and the neighbor *ortho* NO_2 group (with the 5O atom acting as proton acceptor). Notoriously, in the red polymorph this hydrogen bond is bifurcated, the 1N–1H proton being shared by two 5O atoms, one pertaining to the same molecule (intramolecular bond) and the other to a symmetry related 5O atom of a neighbor molecule, the intermolecular bond being much weaker than the intramolecular bond as inferred from the observed D–H and D···A distances (D and A representing the proton donor and acceptor atoms). In addition to the hydrogen bonds involving the bridging N–H group, inspection of the intermolecular distances shows several short C–H···O distances with a suitable geometry that may qualify them as weak hydrogen bond interactions (see Table 5).

In the monoclinic polymorph (Y), the molecules are joined by these weak hydrogen bonds in an extensive 3D pattern (see Figure 9). In the orthorhombic (O) polymorph, the hydrogen bond pattern joins the molecules in chains running along the crystallographic *b*-axis, the structure consisting of a stacking of these chains. In the case of the triclinic (R) polymorph, centrosymmetric pairs of molecules joined by the bifurcated 1N–1H···5O bonds propagate in chains running along the [111] direction, the dimers being joined by weaker C–H···O bonds.

Table 5 – Hydrogen bonds and short intermolecular contacts for the polymorphs of TMA.[a]

Polymorph	D–H···A	D–H/ Å	H···A/ Å	D···A/ Å	< D–H···A/ º
Y	1N−1H···5O	0.83(3)	2.07(3)	2.701(4)	133(3)
Y	6C−6H···2O[a]	0.93	2.46	3.222(3)	139
Y	11C−11H···3O[b]	0.93	2.42	3.325(5)	163
Y	13C−13$_B$H···5O[c]	0.96	2.60	3.415(5)	144
O	1N−1H···5O	0.90(4)	1.89(4)	2.649(4)	141(3)
O	1N−1H···1O[f]	0.90(4)	2.42(4)	3.085(4)	131(3)
O	6C−6H···5O[g]	0.93	2.56	3.480(5)	169
O	8C−8H···4O[h]	0.93	2.56	3.373(5)	147
R	1N−1H···5O	0.85(3)	1.97(3)	2.633(3)	135(3)
R	1N−1H···5O[d]	0.85(3)	2.56(3)	3.197(3)	151(3)
R	6C−6H···2O[e]	0.93	2.43(3)	3.322(3)	163

Symmetry codes: a) 1–*x*, –*y*,1–*z*; b) –*x*, –1/2+*y*,3/2–*z*; c) *x*,1+*y*,*z*; d) –*x*,2–*y*,1–*z*; e) 2–*x*,1–*y*,1–*z*; f) *x*, –1+*y*,*z*; g) 1/2–*x*,1/2+*y*,1/2+*z*; h) *x*,*y*,1+*z*

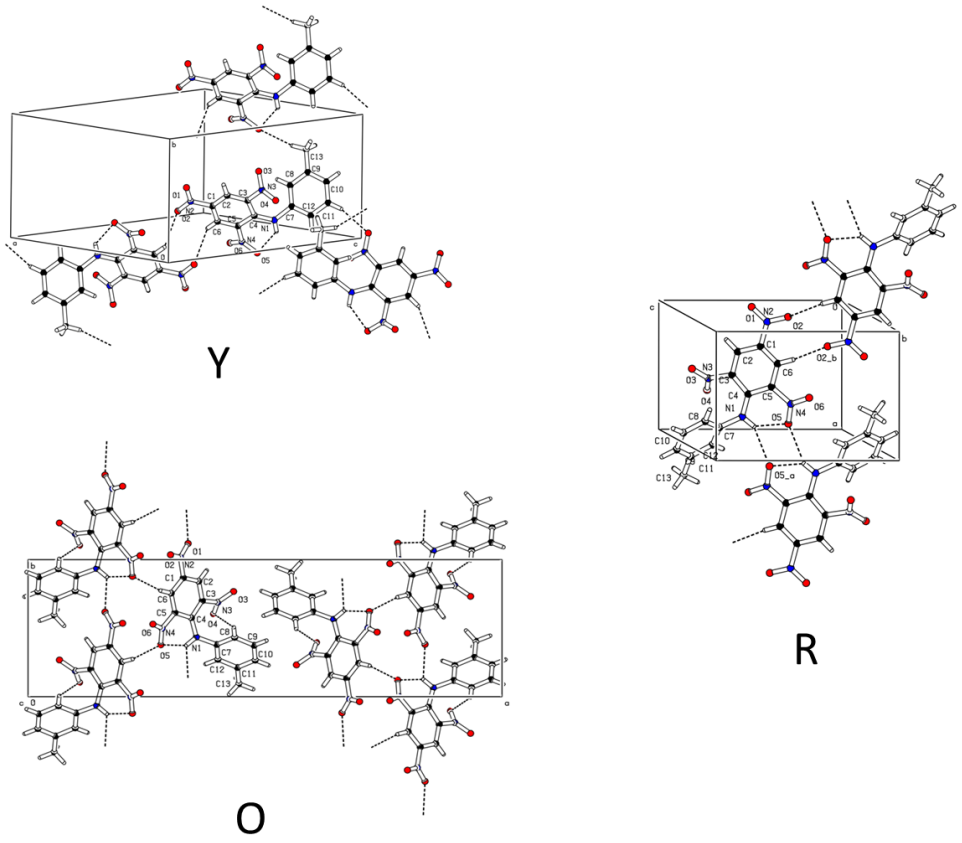

Figure 9 – Hydrogen-bonding network in the monoclinic (Y), orthorhombic (O) and triclinic (R) polymorphs of TMA. In the case of the orthorhombic crystal, the view is a projection of the structure along the *c*-axis.

3.4. Hirshfeld surfaces analysis of the polymorphs

The analysis of molecular crystal structures based on Hirshfeld surfaces, developed by Spackman and co-workers, is a powerful, elegant way to interpret intermolecular interactions in a crystal and to analyze crystal packing.[44,45] In this study, we used this approach to compare the structures of the three polymorphs of TMA. The analysis was performed using CrystalExplorer 17.5,[46] based on the structure input files of the polymorphs (in CIF format). The results are summarized using maps of the normalized contact distance, d_{norm}, on the calculated Hirshfeld surfaces, and the corresponding 2D-fingerprint plots. d_{norm} is calculated from the distances of a given point of the surface to the nearest atom outside, d_e, and inside, d_i, the surface, as defined by Eq. 1 (where r_i^{vdW} are the van der Waals radii), and allows the identification of the regions of the molecule where intermolecular interactions are more relevant.[45–47] The 2D-fingerprint plots allow to condense the information about the relative importance of the different combinations of d_e and d_i throughout the surface of the molecule, indicating the types of intermolecular interactions present in the system and also their relative importance, as given by the associated percent areas of the surface.[45,48–50]

$$d_{norm} = \frac{d_i - r_i^{vdW}}{r_i^{vdW}} + \frac{d_e - r_e^{vdW}}{r_e^{vdW}} \quad (1)$$

Figure 10 shows the calculated Hirshfeld surfaces for the Y, O and R polymorphs of TMA, with the respective intermolecular contacts, as given by the d_{norm} values, which vary from –0.25 to 1.31 in the Y polymorph, from –0.15 to 1.38 in the O polymorph, and from –0.25 to 1.18 in the R polymorph. The magnitude of the intervals of d_{norm} values follow the order 1.56 (Y) > 1.53 (O) > 1.43 (R), which is in agreement with the relative densities (Mg m^{-3}) of the crystals 1.496 (Y) < 1.523 (O) < 1.551 (R) (see Table 1). The red spots on the surfaces shown in Figure 10 represent the most important intermolecular interactions (see also Table 5).

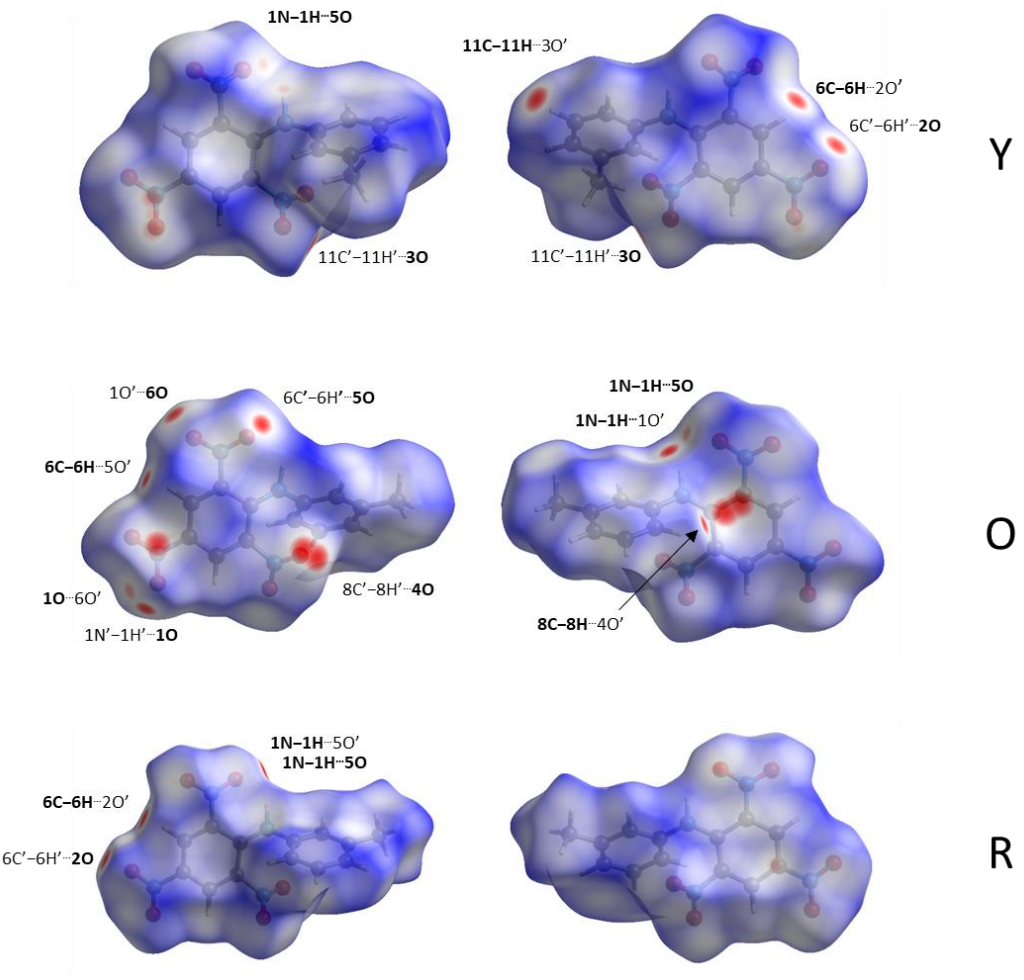

Figure 10 – d_{norm} mapping on the Hirshfeld surfaces of the molecules in the crystals of the three polymorphs of TMA. Two different viewpoints are shown for each molecule (in the left column, with the nitrobenzene group on the left-hand side, and in the right column with the nitrobenzene group on the right-hand side). Atoms participating in the indicating interactions that belong to neighbor molecules are notated using a plica.

Table 6 presents the relative percentages of the Hirshfeld surfaces assigned to the different types of intermolecular interactions, while the corresponding d_e vs. d_i 2D-fingerprint plots are provided as Supporting Information (Figures S10-S12). The H···O/O···H interactions are the prevalent ones in all polymorphs, accounting for ca. 40% of the total interactions. In the O and R polymorphs, where the molecules of TMA are in the B conformation, this type of interaction amounts to 42.7% and 38.6%,

respectively, while in the Y polymorph (made by molecules in the A conformation) it represents 38.2% of the total interactions. The H···C/C···H interactions are also comparatively more important in the O and R polymorphs (12.8% and 14.7%, respectively) than for the Y form (8.9%). On the other hand, the H···H interactions (the second most relevant ones) are more significant in the Y polymorph (22.1%), compared to the O (20.6%) and R (18.2%) forms. These data indicate that the crystal stabilization of the O and R polymorphs is ensured in a higher level both by conventional (H···O/O···H) and non-conventional (H···C/C···H) hydrogen bonding, when compared with the Y form (which is in consonance with the higher density of these crystals as well as with the shorter intervals of their d_{norm} values), while in the Y polymorph dispersive forces are comparatively more important. This latter conclusion is further supported by the larger contributions in the Y polymorph also of O···O and C···C interactions (11.6 and 4.7%, respectively), compared to the O (9.4 and 0.4%) and R (9.7 and 1.7%) forms.

Table 6 – Percent areas of the Hirshfeld surface assigned to the different types of intermolecular interactions in the three polymorphs of TMA.

Interactions	Y	O	R
H···O/O···H	38.2%	38.6%	42.7%
H···H	22.1%	20.6%	18.2%
O···O	11.6%	9.4%	9.7%
H···C/C···H	8.9%	12.8%	14.7%
C···O/O···C	7.3%	10.9%	5.6%
C···C	4.7%	0.4%	1.7%
O···N/N···O	3.8%	3.7%	3.1%
H···N/N···H	2.3%	2.7%	2.3%
C···N/C···H	1.0%	0.7%	1.9%

3.5. Thermal analysis and thermodynamic relationship between the polymorphs

The thermal behavior of the three polymorphs was studied by differential scanning calorimetry (DSC) and by polarized light thermomicroscopy (PLTM). The powder X-ray diffractograms of the polymorphs are shown in Figure S13, where they can be compared with the simulated ones obtained from the single crystal X-ray diffraction data. The two sets of data agree very well, showing that the used materials correspond to the pure polymorphs. The DSC curves are presented in Figure 11 and the values of melting temperature and respective melting enthalpy for each polymorph are presented in Table 7.

From the heat of fusion rule,[51–53] one can conclude that the three TMA polymorphs are enantiotropically related, which means that the orange polymorph is the most stable crystal at the lower temperatures (with all probability including room temperature), and the red and yellow forms

correspond to the most stable forms in intermediate and high temperature ranges. Despite of this enantiotropic relationship, after more than two years of storage at room temperature the transformation of either the Y or R forms into the O polymorph was not observed, which points to a kinetic restriction for such processes at this temperature.

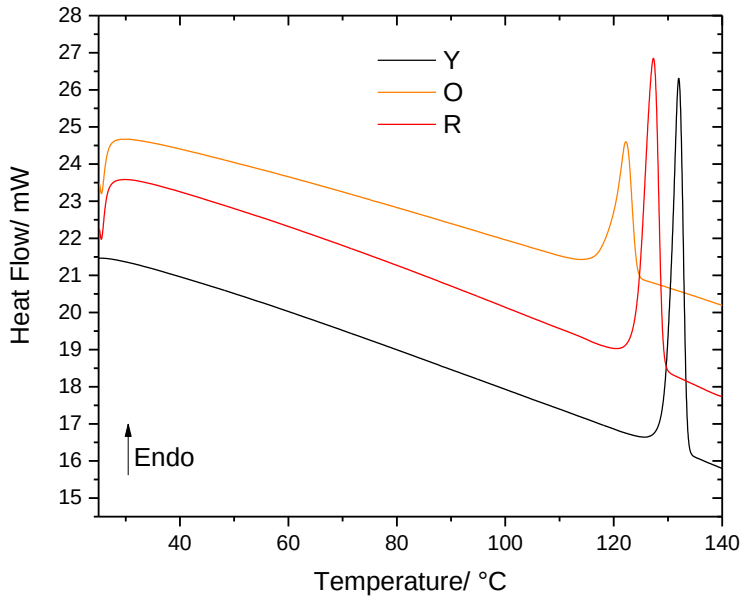

Figure 11 – DSC curves of the Y, O and R polymorphs of TMA (heating rate: 10 ºC min^{-1}). Masses: 2.10 mg (Y), 1.10 mg (O), 2.16 mg (R).

Table 7 – Melting point and enthalpy of fusion for the three polymorphs of TMA.

Polymorph	Melting point/ ºC	Enthalpy of fusion/ kJ mol^{-1}
Y	129.5 ± 0.1	23.1 ± 0.3
O	120.2 ± 0.1	24.6 ± 0.5
R	124.7 ± 0.4	23.7 ± 0.3

The DSC curve of the O polymorph (see Figure 11) is relatively broad, compared to the curves obtained for the other two forms. For that reason, it was decided to study the heating process by PLTM, to visually investigate the melting process of this polymorph. The PLTM images are presented in Figure 12. At 118–120 ºC the sample starts to melt, but the melting process is rather long, with small crystals growing from the melt and then melting again. The temperature of melting of the newly formed crystals (ca. 130 ºC) indicates that they correspond to the yellow TMA polymorph (see Table 7). The formation and subsequent melting of small crystals of either the Y or R polymorphs (or of both) alongside the

melting of the O polymorph crystals could *a priori* explain a broadening of the DSC melting feature observed for the O polymorph. As mentioned above, the PLTM experiments doubtlessly demonstrated that, under the experimental conditions of the thermomicroscopy essays, polymorph Y crystallizes from the melt, while the formation of the R polymorph is uncertain. On the other hand, the observed profile of the DSC melting peak of the O polymorph sample, in particular its end-temperature (ca. 125 ºC; see Figure 11), indicates that in the DSC experiments it is the R polymorph that crystallizes from the melt instead of the Y polymorph.

It is also interesting to note that the melted compound did not crystallize during cooling down till 0 ºC, while the formed glassy phase devitrifies upon heating at around 29 ºC (Figure 13).

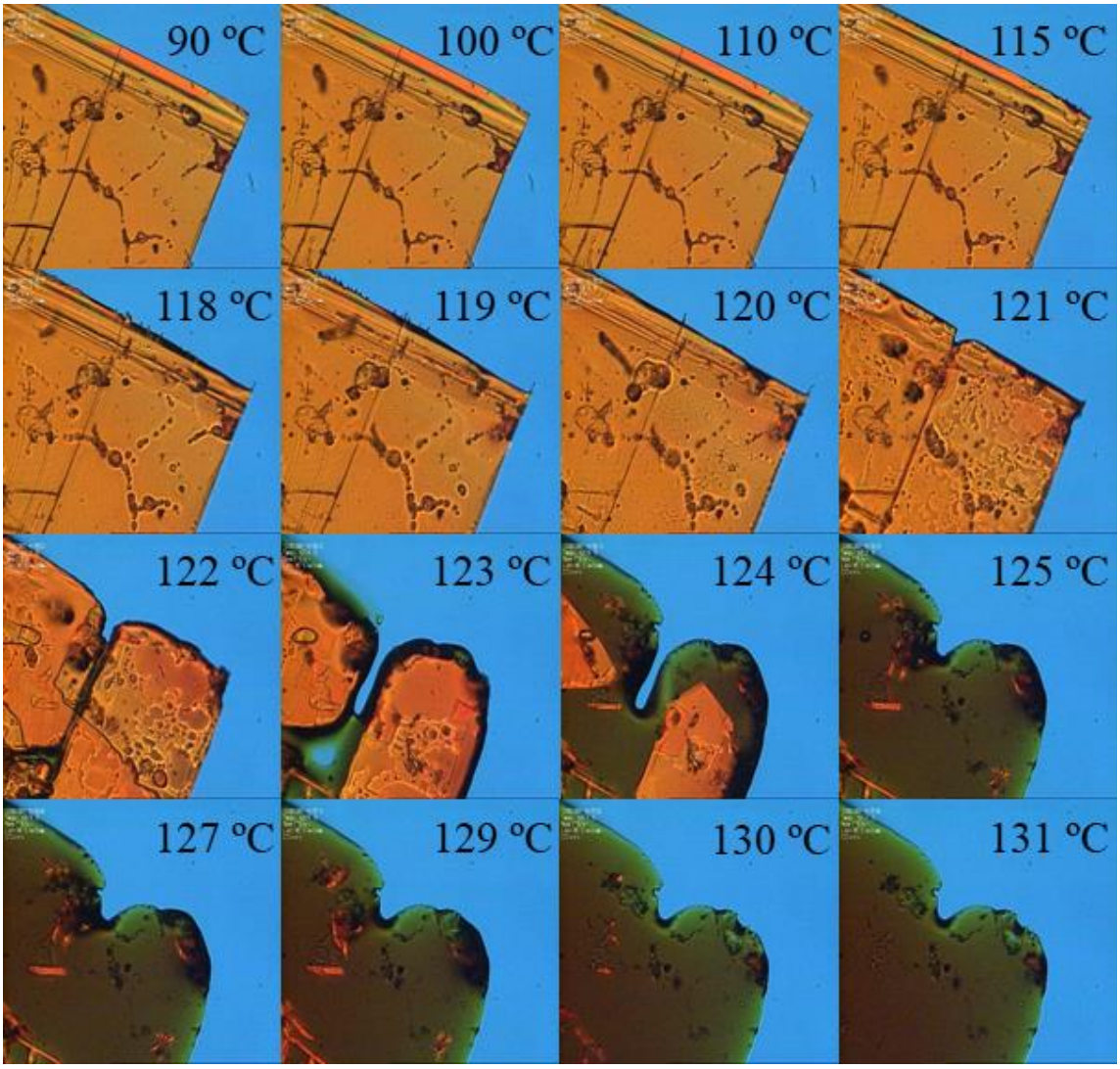

Figure 12 – PLTM images of the heating process of the O polymorph of TMA (heating rate: 10 ºC min^{-1}).

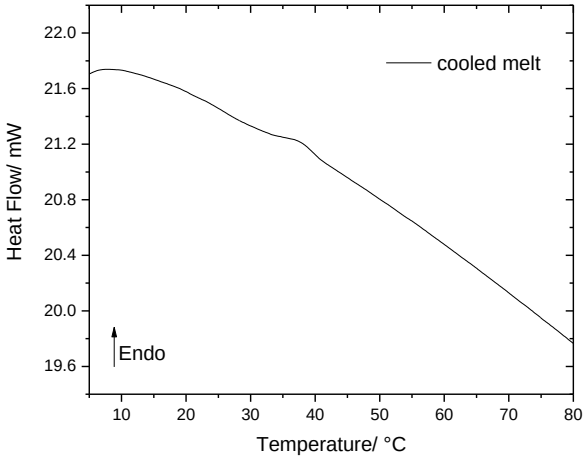

Figure 13 – DSC devitrification curve of a melted sample of TMA (heating rate: 10 ºC min^{-1}).

3.6. Electronic absorption spectra and color of the polymorphs

In order to better understand the origin of the different colors in the three polymorphs of TMA, their UV-vis absorption spectra were collected (Figure14 A). It is clear from the figure that the spectrum of the Y polymorph is considerably different from those of the other two polymorphic forms, which present an overall similar profile. The spectrum of the Y polymorph presents bands with maxima at 274 (UV), 447 (indigo) and 581 (green) nm and shoulders at 330 (UV) and 639 (red) nm, whereas the spectra of the O and R forms show bands with maxima respectively at 316 (UV) and 454 (indigo) nm (O; the band at longer wavelength clearly showing a profile compatible with the coalescence of two bands) and 322 (UV), 446 (violet) and 506 (green) nm (R). In the visible region, the spectral profiles of the different polymorphs have absorption regions compatible with the colors they exhibit (see Figure 5), the color parameters (*x*, *y*) obtained based on the absorption spectra using the CIE 1931 chromaticity scale being (0.338, 0.334), (0.393, 0.367) and (0.432, 0.366) for Y, O and R, respectively (Figure 14 B).

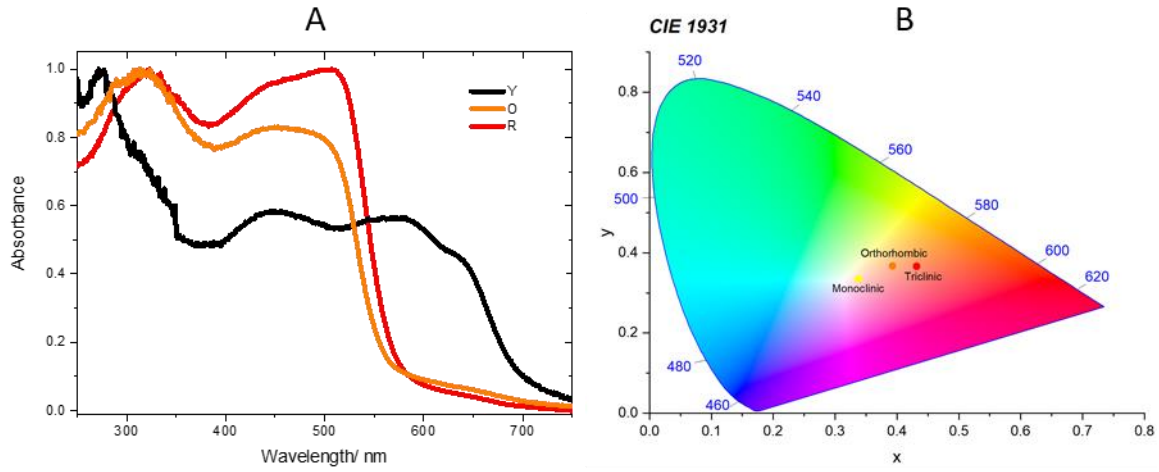

Figure 14 – Normalized solid-state UV-vis absorption spectra of the three polymorphs of TMA, in the 250–750 nm range (A), and the corresponding color parameters in the CIE 1931 chromaticity scale (B).[29]

Considering all the results presented in this study, in particular the spectroscopic data, which are more similar for the O and R polymorph, where the TMA molecules exist in the same (B) conformer, compared to the Y polymorph in which the TMA molecules adopt the A conformation, the different colors of the polymorphs have to be determined in large amount by intramolecular structural features that affect the electronic structure of the chromophore, which corresponds essentially to the picryl moiety. A greater electron donation to the picryl ring shall take place in the R polymorph, and a more reduced one in the Y polymorph, the O form being an intermediate case. The key to understanding the mechanism leading to the different colors is the comparison between the 1N–4C bond lengths in the molecules constituting the different polymorphs. In the Y, O and R polymorphs, this bond length is 1.354, 1.348 and 1.341 Å, respectively, which shows that the extension of the electron donation from 1N to the picryl moiety follows the order R > O > Y, thus explaining the different colors of the polymorphs. The N–C bond length in aniline is 1.355 Å, which is indicative of an increased donation from 1N to 4C in all polymorphs of TMA, due to the presence of the three nitro substituents in the picryl ring of the molecule. On the other hand, the 1N–7C bond in all the TMA polymorphs (Y: 1.421, O: 1.434, R: 1.430 Å) is much longer than that found in aniline and closer to a typical N–C bond length in an amine (ca. 1.469 Å), which indicates that the electron delocalization from 1N to the tolyl moiety of TMA is unimportant. This result is also relevant because, under these conditions, the 1N atom is more available to donate to the picryl ring. Very interestingly, for the conformers of the isolated molecule of TMA, the 1N–4C bond length follows the opposite trend compared to what is observed in the crystals, being shorter in conformer A (1.337 Å) than in conformer B (1.371 Å). This points to the relevance of intermolecular interactions as a major factor in determining the extension of the electron donation from 1N to the picryl ring in the TMA crystals and, thus, ultimately also determining their color even when they correspond to conformational polymorphs (like Y vs. O and R; O and R are packing polymorphs).

4. Conclusion

The color polymorphism exhibited by *N*-picryl-*m*-toluidine (TMA) appears as a fascinating case where both conformational and packing polymorphs exist. As determined by single crystal X-ray diffraction, the yellow polymorph is formed by TMA molecules assuming the conformation of the most stable conformer (A) observed for the isolated molecule of the compound, while both the orange and red polymorphs are formed by conformer B. Interestingly, despite the yellow polymorph presents spectroscopic properties that differ more from those of the orange and red polymorphs, packing appears to be the ultimate cause determining the different colors of all polymorphs, modulating the electronic properties of the chromophore, in particular the electron donation from the amine bridge nitrogen atom to the picryl moiety. This conclusion results from the analysis of the structural data obtained for the isolated molecule and for the crystals, in particular the N–$C_{(picryl)}$ bond length, which is a measure of the

electron delocalization from the bridging N atom to the picryl ring: this bond length correlates inversely with the electron delocalization and it follows the expected order R < O < Y, but it is longer in the isolated conformer B than in conformer A. Also in agreement with this conclusion, the structural data show that the electron delocalization involving the tolyl moiety and the bridge is reduced and that the angle between the two rings (picryl and tolyl) is nearly the same in all crystals.

The Hirshfeld surface analysis for the crystals demonstrates that stabilization of the O and R polymorphs is ensured in a higher level both by conventional (H···O/O···H) and non-conventional (H···C/C···H) hydrogen bonding when compared with the Y polymorph, while in this latter form dispersive forces are comparatively more important. These differences might be in the origin of the different influence of the crystal packing on the electronic properties of the chromophore.

The investigations performed on the TMA isolated molecule allowed to evaluate the major intramolecular interactions determining the conformational preferences of the compound, and characterize its two conformers (A and B) in detail both structurally and vibrationally. The information obtained from these studies were instrumental for the understanding of the structure and properties of the crystals of the different polymorphs.

The infrared and Raman spectra of the different polymorphs were investigated in a comparative basis and fully assigned with help of contemporary fully-periodic DFT calculations on the crystals, while the DSC and PLTM studies allowed to identify the enantiotropic thermodynamic relationship between the polymorphs at normal pressure.

On the whole, this investigation constitutes a comprehensive structural (for both the isolated molecule and crystalline phases), spectroscopic and thermal analysis of TMA, with particular emphasis on the color polymorphism it exhibits.

Supporting Information

Figures S1-S13, with the ^{1}H and ^{13}C NMR spectra of TMA, IR-ATR spectrum of the synthesized material, IR spectrum of the matrix isolated (Ar, 15 K) compound and B3LYP/6-311++G(d,p) calculated spectra its conformers, IR-ATR and Raman spectra of the polymorphs of the corresponding calculated spectra obtained from fully periodic calculations, results of Hirshfeld analysis of the studied crystals, and powder diffractograms (experimental and calculated) for the three polymorphs; Tables S1-S5, with calculated IR spectra of conformers A and B of TMA, and results of the fully-periodic quantum chemical calculations performed on the studied crystals (unit cell parameters of TMA polymorphs, and their IR and Raman spectra). Tables S6-S32 provide structural X-Ray data for the three polymorphs. CIF files containing the supplementary crystallographic data were deposited at the Cambridge Crystallographic Data Centre, with reference CCDC 2100574 (yellow polymorph), 2100587 (red polymorph) and 2100671 (orange polymorph).

Author Contributions

B.A.N. conceptualized the study, wrote a preliminary version of the manuscript and participated in most of the experimental work and in the fully periodic theoretical studies. R.F. contributed to the conceptualization of the study, took responsibility for its supervision and wrote the final version of the manuscript; S.M.M.L. and T.M.V.D.P.M. were responsible for the development of the synthetic route and its implementation; S.L. and T.N. participated in part of the theoretical studies and performed the experimental study of the monomeric compound; A.C.B.R was responsible for the absorption spectroscopy experiments and its interpretation. A.M. and C.C. participated in the full periodic theoretical calculations and the respective interpretation and conclusions; M.E.S.E. participated in the design of the DSC studies; J.A.P. performed the XRD studies and wrote the corresponding section of the manuscript. All authors have participated in the discussion of the results and agreed with the final version of the manuscript.

Acknowledgements

The CQC-IMS is financially supported by the Portuguese Science Foundation ("Fundação para a Ciência e a Tecnologia" - FCT) – Projects CQC UIDB/00313/2020 and UIDP/00313/2020 (National Funds). CFisUC is funded by FCT through the projects UIDB/04564/2020 and UIDP/04564/2020. Access to instruments from Laser-Lab Coimbra and TAIL-UC (ICT_2009_02_012_1890) facilities funded under QREN-Mais Centro is gratefully acknowledged. B.A.N. also acknowledges FCT for the SFRH/BD/129852/2017 PhD Scholarship.

References

1. Nogueira, B. A.; Castiglioni, C.; Fausto, R. Color Polymorphism in Organic Crystals. *Commun. Chem.* **2020**, *3*, 1–12.
2. Bernstein, J. *Polymorphism in Molecular Crystals. International Union of Crystallography Monographs on Crystallography*, Oxford University Press: 2010.
3. Desiraju, G. R. *Crystal Engineering: The Design of Organic Solids*. Elsevier Scientific Publishers: 1989.
4. Cruz-Cabeza, A. J.; Bernstein, J. Conformational Polymorphism. *Chem. Rev.* **2014**, *114*, 2170–2191.
5. Braga, D.; Grepioni, F.; Maini, L.; Polito, M. *Crystal Polymorphism and Multiple Crystal Forms. in Molecular Networks, Structure and Bonding*, Ed. Hosseini, M. W., Vol. 132, Springer: 2009, pp. 87–95.
6. Desiraju, G.; Steiner, T. *The Weak Hydrogen Bond: In Structural Chemistry and Biology, International Union of Crystallography Monographs on Crystallography*, Oxford University Press: 2010.
7. Popelier, P.; Lenstra, A. T. H.; Alsenoy, C.; Van Geise, H. J. An Ab Initio Study of Crystal Field Effects: Solid-state and Gas-phase Geometry of Acetamide. *J. Am. Chem. Soc.* **1989**, *111*, 5658–5660.
8. Cavallini, M.; Calò, A; Stoliar, P.; Kengne; J. C.; Martins, S.; Matacotta, F. C.; Quist, F.; Gbabode, G.; Dumont, N.; Geerts, Y. H.; Biscarini, F. Liquid-Crystal Patterning: Lithographic Alignment of Discotic Liquid Crystals: A New Time-Temperature Integrating Framework. *Adv. Mater.* **2009**, *21*, 4688–4691.
9. Gentili, D.; Durso, M.; Bettini, C.; Manet, I.; Gazzano, M.; Capelli, R.; Muccini, M.; Melucci, M.; Cavallini, M. A Time-temperature Integrator Based on Fluorescent and Polymorphic Compounds. *Sci. Rep.* **2013**, *3*, 2581.
10. Lin, Z.; Mei, X.; Yang, E.; Li, X.; Yao, H.; Wen, G.; Chien, C.-T.; Chow, T. J.; Ling, Q. Polymorphism-dependent Fluorescence of Bisthienylmaleimide with Different Responses to Mechanical Crushing and Grinding Pressure. *CrystEngComm* **2014**, *16*, 11018–11026.
11. Gentili, D.; Gazzano, M.; Melucci, M.; Jones, D.; Cavallini, M. Polymorphism as an Additional Functionality of Materials for Technological Applications at Surfaces and Interfaces. *Chem. Soc. Rev.* **2019**, *48*, 2502–2517.
12. Gattermann, L. Ueber Einige Derivate desm-Nitro-*p*-Toluidins. *Ber. Dtsch. Chem. Gesel.* **1885**, *18*, 1483–1488.
13. Krivoruchka, I. G.; Vokin, A. I.; Aksamentova, T. N.; Shulunova, A. M.; Sorokin, M. S.; Dubinskaya, E. I.; Turchaninov, V. K. Solvatochromism of Heteroaromatic Compounds: XXII.1 Effect of Bifurcate Hydrogen Bond on the IR Spectrum and Dipole Moment of *N*-(4-Methyl-2

nitrophenyl)acetamide in Solution. *Russ. J. Org. Chem.* **2004**, *74*, 120–127.

14. Hantzsch, A. Über Chromoisomerien. *Zeitsch. Angew. Chem.* **1907**, *20*, 1889–1892.
15. Richardson, M. F.; Yang, Q. -C; Novotny-Bregger, E.; Dunitz, J. D. Conformational Polymorphism of Dimethyl 3,6-dichloro-2,5-dihydroxyterephthalate. II. Structural, Thermodynamic, Kinetic and Mechanistic Aspects of Phase Transformations among the Three Crystal Forms. *Acta Cryst. B* **1990**, *46*, 653–660.
16. Stephenson, G. A.; Borchardt, T. B.; Byrn, S. R.; Bowyer, J.; Bunnell, C. A.; Snorek, S. V.; Yu, L. Conformational and Color Polymorphism of 5-Methyl-2-[(2-nitrophenyl)amino]-3-thiophenecarbonitrile. *J. Pharm. Sci.* **1995**, *84*, 1385–1386.
17. Li, X.; Ou, X.; Rong, H.; Huang, S.; Nyman, J.; Yu, L.; Lu, M. The Twelfth Solved Structure of ROY: Single Crystals of Y04 Grown from Melt Microdroplets. *Cryst. Growth Des.* **2020**, *20*, 7093–7097.
18. Busch, M.; Pungs, E. Über Isomere Verschiedenfarbige Pikrylamine. *J. Prakt. Chem.* **1909**, *79*, 546–554.
19. Yaji, T.; Isoda, S.; Kobayashi, T.; Taguchi, K.; Takada, K.; Yasui, M.; Iwasaki, F. Color Change Due to Phase Transition in *N*-(2,4-Dinitrophenyl)-*o*-Anisidine. *Mol. Cryst. Liq. Cryst.* **1999**, *327*, 57–60.
20. Dohmen, C.; Ihmels, H.; Kreienmeier, R.; Patrick, B. O. Synthesis of a Crystallochromic Indolizine Dye by a Base- and Catalyst-free Photochemical Route. *Chem. Commun.* **2019**, *55*, 11071–11074.
21. Kitamura, C.; Ohara, T.; Kawatsuki, N.; Yoneda, A.; Kobayashi, T.; Naito, H.; Komatsu, T.; Kitamura, T. Conformational Polymorphism and Optical Properties in the Solid State of 1,4,7,10-Tetra(n-butyl)tetracene. *CrystEngComm* **2007**, *9*, 644–647.
22. Cullinane, N. M.; Embrey, O. E.; Davis, D. R. Investigation of the Differently Colored Forms of Certain Derivatives of Diphenylamine. *J. Phys. Chem.* **1932**, *36*, 1434–1448.
23. Wood, R. G.; Ayliffe, S. H.; Cullinane, N. M. XXXIII. A Crystallographic and X-ray Investigation of Some Diphenylamine Derivatives. *Mag. J. Sci.* **1935**, *19*, 405–416.
24. Yasui, M.; Taguchi, K.; Iwasaki, F. Dynamic Behavior of *N*-(2,4-Dinitrophenyl)-*o*-anisidine Crystals. *Mol. Cryst. Liq. Cryst.* **1996**, *277*, 167–176.
25. Braun, D. E.; Gelbrich, T.; Jetti, R. K. R.; Kahlenberg, V.; Price, S. L.; Griesser, U. J. Colored Polymorphs: Thermochemical and Structural Features of *N* -Picryl- *p*-toluidine Polymorphs and Solvates. *Cryst. Growth Des.* **2008**, *8*, 1977–1989.
26. Ilyina, I. G.; Mikhalev, O. V.; Butin, K. P.; Tarasevich, B. N.; Uzhinov, B. M. Differently Colored Crystalline Modifications of Organic Autocomplexes of the Nitroaromatic Type. *Synth. Metals* **2001**, *120*, 1067–1068.
27. Sheldrick, G. M. Crystal Structure Refinement with SHELXL. *Acta Cryst.* C71, **2015**, *5*, 3–8.
28. Law, D. P.; Blakeney, A. B.; Tkachuk, R. The Kubelka–Munk Equation: Some Practical

Considerations. *J. Near-Infrared Spectrosc.* **2017**, *4*, 189–193.

29. Smith, T.; Guild, J. The C.I.E. Colorimetric Standards and their Use. *Trans. Opt. Soc.* **1931**, *33*, 73.
30. Frisch, M. J.; Trucks, G. W.; Schlegel, H. B.; Scuseria, G. E.; Robb, M. A.; Cheeseman, J. R.; Scalmani, G.; Barone, V.; Mennucci, B.; Petersson, G. A. *et al.* Gaussian 09 (Revision D.01) Gaussian, Inc. Wallingford (CT, USA), 2009.
31. Becke, A. D. Density-functional Exchange-energy Approximation with Correct Asymptotic Behavior. *Phys. Rev. A* **1988**, *38*, 3098–3100.
32. Lee, C.; Yang, W.; Parr, R. G. Development of the Colle-Salvetti Correlation-energy Formula into a Functional of the Electron Density. *Phys. Rev. B* **1988**, *37*, 785–789.
33. McLean, A. D.; Chandler, G. S. Contracted Gaussian Basis Sets for Molecular Calculations. I. Second Row Atoms, Z = 11–18. *J. Chem. Phys.* **1980**, *72*, 5639–5648.
34. Dovesi, R.; Erba, A.; Orlando, R.; Zicovich-Wilson, C. M.; Civalleri, B.; Maschio,L.; Rérat, M.; Casassa, S.; Baima, J.; Salustro, S.; Kirtman, B. Quantum-mechanical Condensed Matter Simulations with CRYSTAL. *Wiley Interdiscip. Rev. Comput. Mol. Sci.* **2018**, *8*, e1360.
35. Dovesi, R.; Saunders, V. R.; Roetti, C.; Orlando, R.; Zicovich-Wilson, C. M.; Pascale, F.; Civalleri, B.; Doll, K.; Harrison, N. M.; Bush, I. J.; D'Arco, P.; Llunell, M.; Causà, M.; Noël, Y.; Maschio, L.; Erba, A.; Rerat, M.; Casassa, S. CRYSTAL17 User's Manual. 2018
36. Adamo, C.; Barone, V. Toward Reliable Density Functional Methods without Adjustable Parameters: The PBE0 Model. *J. Chem. Phys.* **1999**, *110*, 6158–6170.
37. Grimme, S. Accurate Description of van der Waals Complexes by Density Functional Theory Including Empirical Corrections. *J. Comput. Chem.* **2004**, *25*, 1463–1473.
38. Grimme, S. Semiempirical GGA-type Density Functional Constructed with a Long-range Dispersion Correction. *J. Comput. Chem.* **2006**, *27*, 1787–1799.
39. Civalleri, B.; Zicovich-Wilson, C. M.; Valenzano, L.; Ugliengo, P. B3LYP Augmented with an Empirical Dispersion Term (B3LYP-D*) as Applied to Molecular Crystals. *CrystEngComm* **2008**, *10*, 405–410.
40. Merrick, J. P.; Moran, D.; Radom. L., An Evaluation of Harmonic Vibrational Frequency Scale Factors. *J. Phys. Chem. A* **2007**, *111*, 11683–11700.
41. Rathore, B. S.; Gupta, V.; Gupta, R. R.; Kumar, M. Synthesis of 7-Chloro-9-trifluoromethyl-7-fluorophenothiazines. *Heteroat. Chem.* **2007**, *18*, 81–86.
42. Reva, I. D.; Stepanian, S. G.; Adamowicz, L.; Fausto, R., Missing Conformers: Comparative Study of Conformational Cooling in Cyanoacetic Acid and Methyl Cyanoacetate Isolated in Low Temperature Inert Gas Matrixes, *Chem. Phys. Lett.* **2003**, *374*, 631–638.
43. Domenicano, A.; Vaciago, A.; Coulson, C. A. Molecular Geometry of Substituted Benzene Derivatives. I. On the Nature of Ring Deformations Induced by Substitution. *Acta Cryst.* **1975**, *B31*, 221–234.

44. Spackman, M. A.; Byrom, P. G. A Novel Definition of a Molecule in a Crystal. *Chem. Phys. Lett.* **1997**, *267*, 215–220.
45. Spackman, M. A.; Jayatilaka, D. Hirshfeld Surface Analysis. *CrystEngComm* **2009**, *11*, 19–32.
46. Wolff, S. K.; Grimwood, D. J.; McKinnon, J. J.; Turner, M. J.; Jayatilaka, D.; Spackman, M. A. Crystal Explorer17 (version 17.5), University of Western Australia, Crawley (AUS), 2017.
47. McKinnon, J. J.; Mitchell, A. S.; Spackman, M. A. Hirshfeld Surfaces: A New Tool for Visualising and Exploring Molecular Crystals. *Chem. - A Eur. J.* **1998**, *4*, 2136–2141.
48. Spackman, M. A.; McKinnon, J. J. Fingerprinting Intermolecular Interactions in Molecular Crystals. *CrystEngComm* **2002**, *4*, 378–392.
49. Rohl, A. L.; Moret, M.; Kaminsky, W.; Claborn, K.; McKinnon, J. J.; Kahr, B. Hirshfeld Surfaces Identify Inadequacies in Computations of Intermolecular Interactions in Crystals: Pentamorphic 1,8-Dihydroxyanthraquinone. *Cryst. Growth Des.* **2008**, *8*, 4517–4525.
50. Parkin, A.; Barr, G.; Dong, W.; Gilmore, C. J.; Jayatilaka, D.; McKinnon, J. J.; Spackman M. A.; Wilson, C. C. Comparing Entire Crystal Structures: Structural Genetic Fingerprinting. *CrystEngComm* **2007**, *9*, 648–652.
51. Burger, A.; Ramberger, R. On the Polymorphism of Pharmaceuticals and other Molecular Crystals. I - Theory of Thermodynamic Rules. *Mikrochim. Acta* **1979**, *72*, 259–271.
52. Burger, A.; Ramberger, R. On the Polymorphism of Pharmaceuticals and other Molecular Crystals. II - Applicability of Thermodynamic Rules. *Mikrochim. Acta* **1979**, *72*, 273–316.
53. Yu, L. Inferring Thermodynamic Stability Relationship of Polymorphs from Melting Data. *J. Pharm. Sci.* **1995**, *84*, 966–974.

For Table of Contents Use Only

2,4,6-Trinitro-*N*-(*m*-tolyl)aniline: A New Polymorphic Material Exhibiting Different Colors

Bernardo A. Nogueira,[1,2,*] Susana M. M. Lopes,[1] Susy Lopes,[1] Timur Nikitin,[1]
Ana Clara B. Rodrigues,[1] Maria Ermelinda S. Eusébio,[1] José A. Paixão,[3]
Teresa M. V. D. Pinho e Melo,[1] Alberto Milani,[2] Chiara Castiglioni[2] and Rui Fausto[1]

[1] *University of Coimbra, CQC-IMS, Department of Chemistry, P-3004-535 Coimbra, Portugal.*
[2] *CMIC, Dipartimento di Chimica, Materiali e Ingegneria Chimica "G. Natta", Politecnico di Milano, Italy.*
[3] *University of Coimbra, CFisUC, Department of Physics, P-3004-516 Coimbra, Portugal*

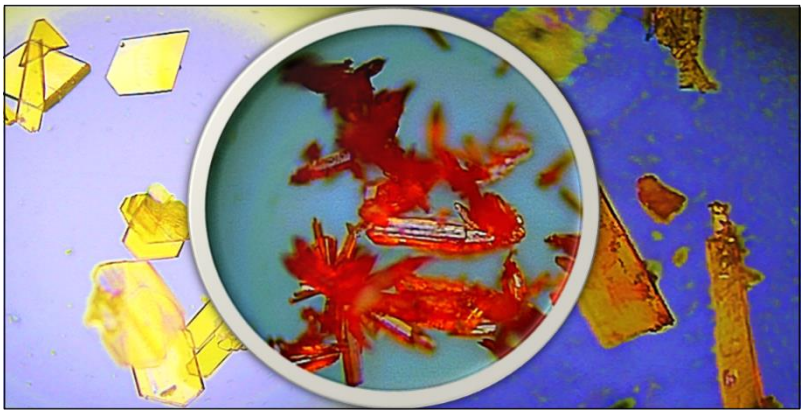

A comprehensive structural (for both the isolated molecule and crystalline phases), spectroscopic and thermal investigation of a novel compound exhibiting color polymorphism is presented. The yellow polymorph is a conformational polymorph of the orange and red ones, while the last two are packing polymorphs. Mechanistic insights on the causes of the different colors of the polymorphs are presented.